Two-way interaction between solid particles and homogeneous air turbulence: particle settling rate and turbulence modification measurements

By T. S. YANG and S. S. SHY†

Department of Mechanical Engineering, National Central University, Jhongli 32054, Taiwan

This paper describes experiments on small solid particle settling behaviour in stationary homogeneous isotropic air turbulence. We present here a new methodology using a recently developed cruciform apparatus: a large horizontal cylindrical vessel equipped with a pair of counter-rotating fans and perforated plates at each end is used to generate stationary near-isotropic turbulence in the core region between the two perforated plates and a long vertical vessel is used to supply heavy descending particles from its top. This novel experimental design, without the unwanted influences from the injection of particles, the mean flow, and the decay of turbulence, allows direct imaging and velocity measurements of the two-way interaction between heavy particles and homogeneous isotropic turbulence. Consequently, the spatiotemporal responses of both fluid turbulence and particle settling can be determined by high-speed digital particle image velocimetry and accelerometry, together with the wavelet transform analysis for the first time. Hence, experimental information on and thereby understanding of the particle settling rate, preferential accumulation, and turbulence modification due to the presence of the particles is obtained.

We found that the particle settling velocity (V_s) is much greater than the terminal velocity (V_t) in still fluid for which the value of ($V_s - V_t$) reaches a maximum of $0.13u'$ when the Stokes number $St = \tau_p/\tau_k \approx 1$ and $V_t/u' \approx 0.5$ at $Re_\lambda = 120$ and $Re_p < 1$, in good agreement with previous numerical results, where τ_p is the particle's relaxation time, τ_k is the Kolmogorov time scale, u' is the energy-weighted r.m.s. turbulent intensity, and Re_λ and Re_p are the Reynolds numbers based on the Taylor microscale (λ) and the mean diameter of particles, respectively. Non-uniform particle concentration fields are observed and most significant when $St \approx 1.0$, at which the particle clusters accumulate preferentially around the outer perimeter of small intense banana-shaped vortical structures. These clusters can turn and stretch banana-shaped vortical structures toward the gravitational direction and thus significantly increase the mean settling rate especially when $St = 1$. From spatiotemporal analysis of the flatness factor, it is found that the characteristic length and time scales of these preferential particle clusters are related to the spacing between the adjacent intense vorticity structures of the order λ and the time passage of these clustering structures of the order τ_k, respectively. By comparing the average frequency spectra between laden (heavy particle) and unladen (neutral particle) turbulent flows over the measurement field at a fixed $Re_\lambda = 120$, turbulence augmentation is found for most frequencies in the gravitational direction, especially for $St \geqslant 1$. In the transverse direction, augmentation occurs only at higher frequencies beyond the Taylor microscale for all values of St studied varying from 0.36 to 1.9. The increase in the size of energy spectra (turbulence

† Author to whom correspondence should be addressed: sshy@cc.ncu.edu.tw

augmentation) due to the presence of heavy particles is greatest at τ_k^{-1} when $St \approx 1.0$. Furthermore, the slip velocities between fluid turbulence and heavy particles can stimulate the laden turbulent flow to become more intermittent in the dissipation range. Finally, a simple energy balance model for turbulence modification is given to explain these results and areas for further study identified.

1. Introduction

Knowledge of the dispersion and the settling of heavy particles in turbulence is central in many natural and industrial flows. Consider small heavy particles as point forces interacting with turbulence. Upon descending, these point forces would exert a force on the fluid which competes with the drag the fluid exerts on them, leading to phenomena quite different from those of unladen turbulent flows. Examples are as diverse as mixing of sprays in a combustor, the collection of particles in an electrostatic precipitator, sediment grains in rivers, and aerosol particles in the atmosphere. This paper presents a new methodology to study experimentally gravitational settling rates and turbulence modification of solid particles in stationary homogeneous isotropic air turbulence.

In the past, the dispersion of heavy particles in turbulence, including the Lagrange particle velocity autocorrelation function, the turbulent diffusivity of particles and fluid points, particle response and turbulence modification, and the preferential concentration field of particle dispersion patterns, has been extensively and carefully studied (see Snyder & Lumley 1971; Wells & Stock 1983; Maxey & Riley 1983; Longmire & Eaton 1992; Elghobashi & Truesdell 1993; Schreck & Kleis 1993; Kulick, Fessler & Eaton 1994; Kiger & Lasheras 1995; Yang, Crowe & Chung 1995; Crowe, Troutt & Chung 1996, among others). Most of these experiments were carried out either in simple free shear flows or in decaying homogeneous turbulence generated in wind and water tunnels. On the other hand, very few experimental results are available on settling, because the particles would be influenced by the mean flow, making the determination of the settling velocity uncertain. Currently, only numerical simulations are available for the settling velocity of heavy particles in stationary homogeneous isotropic turbulence without any mean flow (see Wang & Maxey 1993; Mei 1994; Yang & Lei 1998). However, these simulations do not agree with each other and a number of issues are still not well understood, such as (i) whether turbulence would increase or decrease the average settling velocity, (ii) how the concentration field and the settling of particles are influenced by temporal variation and velocity scaling of turbulence, and (iii) what the modification of fluid turbulence due to the presence of the particles is. Hence, the objective of this work is to address these unsolved issues.

It has been recognized that the fluid mechanics in particle-laden turbulent flows are related to two non-dimensional parameters, namely the Stokes number ($St \equiv \tau_p/\tau_k$, the ratio of the particle response time to the Kolmogorov time scale of turbulence) and a terminal velocity ratio (V_t/v_k or V_t/u', the ratio of the terminal velocity of the particles to a characteristic velocity of fluid turbulence, where v_k and u' are the Kolmogorov velocity and the effective root-mean-square velocity fluctuations of turbulence, respectively). The settling velocity due to the particle–turbulence interaction and the correlation between the preferential concentration and the settling velocity of heavy particles, in the absence of turbulence modification by the addition of

particles, has been thoroughly investigated (Wang & Maxey 1993; Yang & Lei 1998; Aliseda *et al.* 2002). Wang & Maxey (1993) found an increase in the average settling velocity of heavy particles (V_s) due to turbulence compared to the particle terminal velocity in still fluid using direct numerical simulation (DNS). They proposed that the Kolmogorov eddies may play an important role in certain aspects of particle settling in homogeneous isotropic turbulence, for which the significant accumulation by inertial bias (particles accumulating in high-strain-rate and low-vorticity regions) occurs when $St = 1$. However, Yang & Lei (1998) performed an investigation on the role of turbulent scales in the aforementioned problem using both DNS and large-eddy simulation (LES) and pointed out that the Kolmogorov scaling may be inadequate based on the following two reasons. (i) The preferential accumulation of the particles in low-vorticity regions was related to small intense vorticity structures where the length scale corresponding to the maximum of the vorticity spectrum was one order of magnitude greater than the Kolmogorov length scale, η. (ii) The characteristic velocity scale of turbulence for the particle accumulation in the region of low vorticity was u', not v_k, since the large energetic eddies may play a significant role in the local drag of the particles. In contrast to the enhancement of the mean settling velocity ($V_s > V_t$) found by the aforementioned simulations, Mei (1994) investigated the particle settling velocity in both linear and nonlinear drag regimes in low-Reynolds-number isotropic turbulence using Monte Carlo simulation. Mei reported that turbulence may have little influence on the particle settling velocity in the linear Stokes drag regime when the particle Reynolds number $Re_p = u'd_p/\nu$ was less than unity, where d_p was the particle diameter. In addition, Mei also predicted that values of V_s may even become less than V_t when the nonlinear drag law ($Re_p > 1$) was applied.

Recently, Aliseda *et al.* (2002) investigated experimentally the effect of preferential concentration on the settling velocity of water droplets in decaying wind-tunnel grid turbulence. They found that mass loading effects are important, for which values of V_s are much greater than V_t and may increase linearly with the particle volume fraction ($\alpha = 1.5$–7.0×10^{-5}) at a fixed St. However, in their experiment the turbulent intensity (u') used for characterization was very small compared to the mean velocity of the flow, where u' was only about 2% of the mean axial velocity at the centre of the wind tunnel at the location $x = 100$ cm (see figure 6 of Aliseda *et al.* 2002). In addition, u' decayed rapidly with x. If the particles that are carried by the strong mean axial flow do not reach their terminal velocity, do not have sufficient settling distance in the gravitational direction, and are not free from the influence of the rapid decay of turbulent intensity, the determination of the settling velocity in decaying turbulence is very difficult to achieve. Another relevant experiment by Yang & Shy (2003) reported measurements of the settling velocity of solid particles in aqueous stationary isotropic turbulence that was generated by a pair of vertically vibrating grids in a water tank. They found that $V_s > V_t$ and $(V_s - V_t)/V_t$ reaches its maximum of about 7% around $St \approx 1$, even when Re_p is as large as 25 at which $V_t/v_k \approx 10$. However, because of the experimental limitations for vibrating-grids turbulence, Yang & Shy were unable to study the parameter ranges $Re_p < 1$ and $V_t/v_k = 1$–6 where the enhancement of the settling velocity may be most significant. Hence, there is a need to devise an idealized turbulent flow system and apply a better measuring method for benchmark experimental data on the settling velocity.

The ideal turbulent flow system is one in which small heavy particles descend with their terminal velocity through three-dimensional fully developed stationary isotropic turbulence with zero mean velocities. Thus, these particles are not influenced by the mean flow, the unwanted disturbances from the injection of the particles, and the

decay of turbulence. In addition, the test section and/or the measuring field must be large enough so that particle–turbulence interactions can occur over many turbulent integral length scales in all three directions. In this study, we propose to use a gaseous cruciform apparatus, consisting of a long vertical vessel for providing uniform distribution of descending heavy particles with terminal velocity and a large horizontal vessel for generating stationary near-isotropic turbulence, which satisfies most of the aforementioned conditions. This cruciform apparatus was recently applied to investigate the behaviour of premixed flames propagating in intense isotropic turbulence for a premixed turbulent combustion study (Shy *et al.* 2000*b*; Shy, Lin & Peng 2000*c*; Shy, Lin & Wei 2000*d*; Chang *et al.* 2001; Yang & Shy 2002). This closed turbulent flow system can be used to study particle–turbulence interactions at reduced, normal, and elevated pressures from 0.01 atm to 5 atm. This paper discusses only cases conducted at normal pressure (1 atm). In order to investigate both spatial and temporal responses of fluid turbulence as well as particle settling in turbulence, high-speed, digital particle image velocimetry (DPIV) together with the wavelet transform analysis is employed. Thus, the settling velocity, the evolution of the concentration field, and the spatiotemporal response of heavy particles due to stationary near-isotropic turbulence can be scrutinized.

Another important issue which is still not well-understood is the turbulence modification due to the particle–fluid coupling, the so-called two-way or phase coupling. The addition of heavy particles to a turbulent flow can modify the transport of mass, momentum and energy of the turbulence and thus influence the motion of the particles, see Crowe (1991), Elghobashi & Truesdell (1993), Crowe *et al.* (1996), among others. There is still no general consensus on whether the addition of particles would increase or decrease the turbulent kinetic energy of the carrier fluid. For instance, Fessler & Eaton (1999) found the attenuation of streamwise fluid turbulence in the channel-flow extension region of a backward-facing step flow, but Sato *et al.* (1995) reported turbulence augmentation in the low-wavenumber region in water channel flow turbulence due to the presence of the heavy particles. Using DNS, Elghobashi & Truesdell (1993) studied the modification of decaying homogeneous turbulence due to its interaction with dispersed small solid particles for a volumetric loading ratio $\alpha \leqslant 5 \times 10^{-4}$. They found that the particles can transfer their momentum to the small-scale motion of fluid turbulence in an anisotropic manner because gravity acts in one direction; the higher the gravity the larger the anisotropy. This paper reports experimental measurements of turbulence modification due to descending heavy particles for the first time. The focus is on the intermittency of small intense laden fluid vorticity structures, the characteristic length and time scales of preferentially accumulated particle clusters, and the wavelet energy spectra in the frequency domain for both transverse and gravitational directions of particle-laden turbulent flow.

The following section reviews experimental methods used in the study, followed by descriptions of measurements of the velocity fields for both fluid turbulence and heavy settling particles using the high-speed DPIV technique and the corresponding acceleration fields, and multi-resolution statistical diagnostics using the wavelet analysis. All three are then employed to extract the mean particle settling velocity, the spatio-temporal evolution of the particle concentration field, the characteristic scales of turbulent laden flow, and turbulence modification due to the presence of descending heavy particles. A simple model for turbulence modification is proposed to explain the production of turbulent kinetic energy of the laden fluid due to the external volume force of the particle drag. Finally, conclusions are offered and areas for further study identified.

2. Experimental methods

2.1. *Flow facility and particle feeder*

The flow facility has been described previously (see Shy *et al.* 2000*d*). For complete-ness, we briefly summarize the setup and describe the new modification that we employ in order to study the two-way interaction between solid particles and stationary near-isotropic turbulence. Figure 1 shows the cruciform apparatus that consists of two cylindrical vessels. The large horizontal vessel was equipped with a pair of counter-rotating fans and perforated plates at each end to generate stationary near-isotropic turbulence in the core region between the two perforated plates, as verified by extensive LDV measurements (Shy, I & Lin 2000*a*). In this near-isotropic region of about $15 \times 15 \times 15$ cm^3 volume, mean velocities are approximately negligible and r.m.s. turbulent intensities in all three directions are nearly the same. This uniform region of turbulence can contain many large eddies for large numbers of interactions with descending heavy particles. Three large quartz windows 10 cm in diameter were posi-tioned at the front and the back of the central region of the large horizontal vessel as well as at the bottom of the long vertical vessel for DPIV measurements (see figure 1). In this study, two different measuring fields of view are selected (3.14 cm $\times$ 2.75 cm and 5.84 cm $\times$ 5.11 cm), which are located in the middle of the near-isotropic region to minimize the boundary influence from the walls of the cruciform chamber. We will present flow turbulence statistics obtained from high-speed DPIV measurements, including velocity and vorticity field maps, energy spectra, and the flatness factor as a function of length scale and frequency, and these results will be compared with the results obtained in the particle-laden cases in an attempt to investigate the issue of turbulence modification.

One challenge of the present study is to distribute heavy descending particles uniformly and continuously through the region of interest for measurements of the two-way interaction using high-speed DPIV. After many tests, the most satisfactory method is to use a specially designed particle feeder which is placed on the top of the long vertical vessel at a distance of about 1 m from the central uniform region (figure 1). Inside the particle feeder, there is a frequency-controllable shaking box driven by an eccentric DC motor. The box contains a large number of selected particles with a fixed mean diameter and the bottom is made up of two overlapping nets of small meshes. When the box is shaken by the eccentric motor, the seeding particles required for both unladen and laden cases can be generated, on which to perform DPIV measurements at reduced and elevated pressures from 0.01 atm to 5 atm. Note that these descending heavy particles have reached the terminal velocity before interacting with turbulence, and most importantly they are not influenced by the mean flow and unwanted disturbances from a particle injection process.

For the unladen case, the flow is seeded with aluminium powder of 0.3 µm in mean diameter that possess the ability to follow the response of fluid turbulence ($\tau_p \ll \tau_k$) and thus can be used to measure fluid velocity and vorticity maps using DPIV. It should be noted that the DPIV image quality using the present seeding method is very good only when the fan frequency (f) is below 12 Hz at which the fan Reynolds number $Re_{fan} = f D_f L_I / \nu$ is about 2800. D_f is the fan diameter of 11.6 cm, L_I is the integral length scale of turbulence, and ν is the kinematic viscosity of air. Hence, the highest fan frequency f is set at 10 Hz in this study to obtain the best particle image quality for DPIV processing, even though the two counter-rotating fans can be operated up to 172 Hz via the two frequency converters (Yang & Shy 2002). Table 1 lists fluid turbulence properties, where L_I and τ_I are the integral length and time
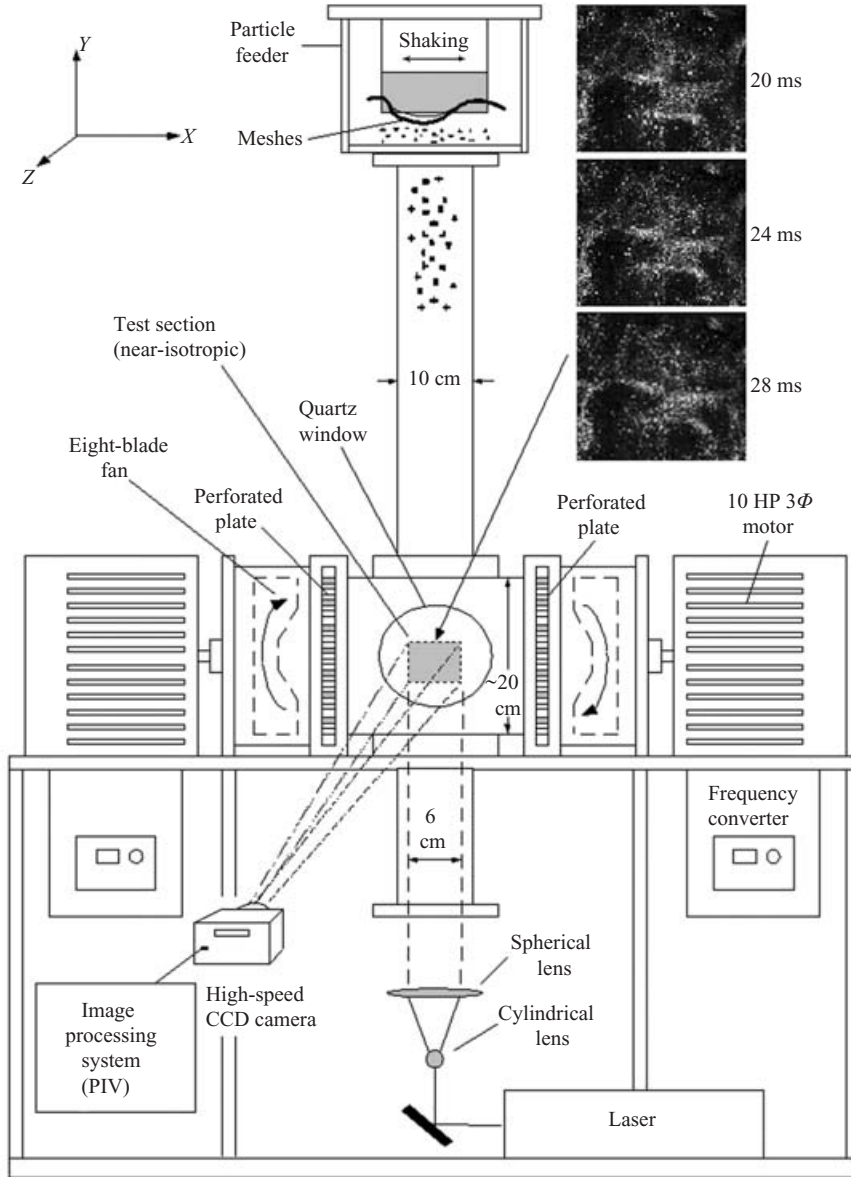
FIGURE 1. Schematic diagram of the cruciform apparatus with the DPIV image acquisition arrangement. The particle feeder on the top of the long vertical vessel contains selected heavy particles in a horizontally vibrating box with appropriate meshes below, such that the required gravitationally descending particles can be provided at reduced, normal, and elevated pressures. On the right, there are three instantaneous laser sheet images at three sequential times taken from the test section, with copper particles with a mean diameter of $d_p \approx 12\,\mu\mathrm{m}$ and fan frequency of $f = 7\,\mathrm{Hz}$, revealing the interaction between solid particles and near-isotropic air turbulence.

scales, λ is the Taylor microscale, and v_k, η and τ_k are the Kolmogorov velocity, length and time scales, respectively: $v_k = (\nu\varepsilon)^{1/4}$, $\eta = (\nu^3/\varepsilon)^{1/4}$, and $\tau_k = (\nu/\varepsilon)^{1/2}$, in which the viscous dissipation rate $\varepsilon = A(u'^3/L_I)$ where A is a constant with value unity (Hinze 1975). Re_t or Re_λ are the turbulent Reynolds numbers based on the

Properties	$f = 5\,\mathrm{Hz}$	$f = 7\,\mathrm{Hz}$	$f = 10\,\mathrm{Hz}$
u' $(\mathrm{cm\,s^{-1}})$	14.1	20.6	30.5
v_k $(\mathrm{cm\,s^{-1}})$	3.24	3.75	4.22
L_I (cm)	1.98	2.63	2.89
λ (cm)	0.77	0.86	0.99
η (cm)	0.046	0.040	0.035
τ_I (s)	0.30	0.24	0.19
τ_k (ms)	14.0	10.7	8.40
ε $(\mathrm{cm^2\,s^{-3}})$	750	1285	2126
$Re_{fan} = f D_f L_I / \nu$	766	1424	2235
$Re_t = u' L_I / \nu$	186	362	590
$Re_\lambda = u' \lambda / \nu$	73.0	120	202

TABLE 1. Fluid turbulence characteristics.

energy-weighted r.m.s. turbulent intensity u', and L_I or λ respectively. Note that ε can be also estimated by $\varepsilon = 15\nu(u'/\lambda)^2$ for isotropic turbulence, and its three-dimensional form $\varepsilon = \nu \partial u_i / \partial x_j (\partial u_i / \partial x_j + \partial u_j / \partial x_i)$ can be simplified into the two-dimensional form $\varepsilon = 6\nu[(\partial u / \partial x)^2 + (\partial u / \partial y)^2 + (\partial u / \partial y)(\partial v / \partial x)]$ (Hinze 1975). For the present fan-stirred near-isotropic turbulence, u' and λ can be directly obtained from DPIV measurements with wavelet analyses. As a typical example for comparison, for the case of $f = 7\,\mathrm{Hz}$ and $Re_\lambda = 120$, then $\varepsilon \approx 1285\,\mathrm{cm^2\,s^{-1}}$ and $1196\,\mathrm{cm^2\,s^{-1}}$ when the relation $\lambda / u' = \sqrt{15}(\nu / \varepsilon)^{1/2}$ and the above two-dimensional form of ε are used, respectively, in which both values of ε are nearly the same, suggesting that the present turbulence has a very high degree of isotropy. Three fan frequencies, $f = 5, 7$, and $10\,\mathrm{Hz}$, are employed, corresponding to values of $Re_\lambda / Re_{fan} = 70/776$, $120/1424$, and $202/2235$, respectively. The vertical turbulent intensity is found to be slightly greater than the horizontal turbulent intensity with a ratio of about 1.08 at $f = 7$ and $10\,\mathrm{Hz}$. These turbulent properties, shown in table 1, are obtained from DPIV measurements as well as the wavelet transform analysis without adopting Taylor's hypothesis, as to be discussed in detail later.

2.2. *Selection of particles*

Concerning the particle-laden case, the appropriate descending heavy particles should have a density $\rho_p \gg \rho_f$ (the fluid density) with a mean particle diameter $d_p \leqslant \eta$ and a terminal velocity $V_t \geqslant v_k$, so that the required conditions of $Re_p < 1, 0 < St < 2$, $1 \leqslant V_t / v_k \leqslant 10$, and $0 \leqslant V_t / u' \leqslant 1.5$ can be achieved. This experimental parameter range matches closely with those used in numerical studies (Wang & Maxey 1993; Yang & Lei 1998), so that a direct comparison between these two different approaches can be made. To achieve this purpose based on the limitation of $f \leqslant 10\,\mathrm{Hz}$, three heavy particles, respectively copper particles with an arithmetic mean diameter of $d_p \approx 12\,\mu\mathrm{m}$, glass particles with $d_p \approx 40\,\mu\mathrm{m}$, and lead particles with $d_p \approx 24\,\mu\mathrm{m}$ are selected, which give $\rho_p / \rho_f \gg 1, 0 < V_t / v_k < 6$, $Re_p < 1$, and $0 < St < 2$. Table 2 shows these three particles' characteristics, where the corresponding values of St are 0.36, 1.0, and 1.9 for copper, glass, and lead particles, respectively. Note that the particle relaxation time is estimated using the relation $\tau_p = (\rho_p / \rho_f - 1)d_p^2 / 18\nu$, where the Stokes drag law is applied because $Re_p < 1$. These selected particles are first carefully sieved through two overlapping nets of small mesh and then examined using many SEM micrographs to estimate their mean diameter in attempt to keep the size distribution as monodispersed as possible. For example, the glass particles are sieved

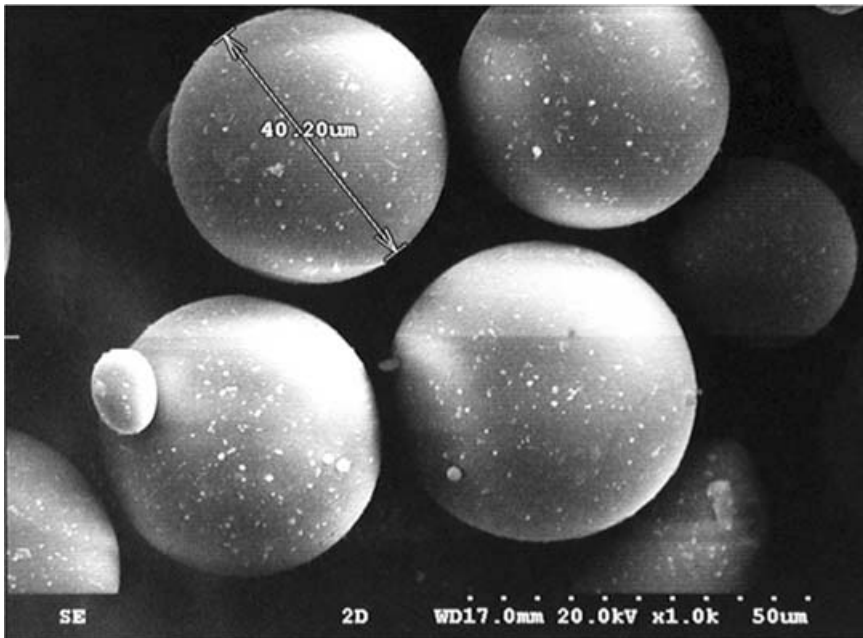| Properties	Copper	Glass	Lead
Arithmetic mean diameter, d_p (µm)	12	40	24
Density, ρ_p (g cm^{-3})	8.80	2.50	11.3
Average relaxation time, τ_p (ms)	3.860	11.56	19.80
Terminal velocity, V_t (cm s^{-1})	3.780	11.33	19.41
Particle Reynolds number, $Re_p = V_t d_p / \nu$	0.0300	0.303	0.312
Stokes number, $St = \tau_p / \tau_k$	0.36	1.0	1.9

TABLE 2. Particle characteristics.

FIGURE 2. A typical SEM micrograph of the glass particles with nominal diameter of $d_p \approx 40\,\mu\text{m}$, which are sieved through 34 µm and 43 µm sieves.

through 34–43 µm sieves many times and a typical SEM micrograph is displayed in figure 2, yielding a mean diameter of about 40 µm with a very small size distribution (less than 10%). However, the copper and lead particles with smaller mean diameters of 12 µm and 24 µm, respectively, have larger size distribution (about 12%–18%), so that their results should be viewed with some caution.

Before a run, the two counter-rotating fans are operated at a fixed frequency to establish the required turbulence. Then the box inside the particle feeder starts to shake at a fixed frequency to release continuously a cloud of aluminum powder of 0.3 µm mean diameter for the unladen case or selected heavy particles for the laden case from the top of the cruciform apparatus. As can be seen from the two pairs of laser sheet images on figure 3, the distribution of particle concentration at the entrance of the 'chamber' between the pair of fans has a very high degree of uniformity with a volume fraction of about 10^{-5}. When the particles have entered the central uniform region in which the particle image concentration is about 15–25 particles in a 32×32
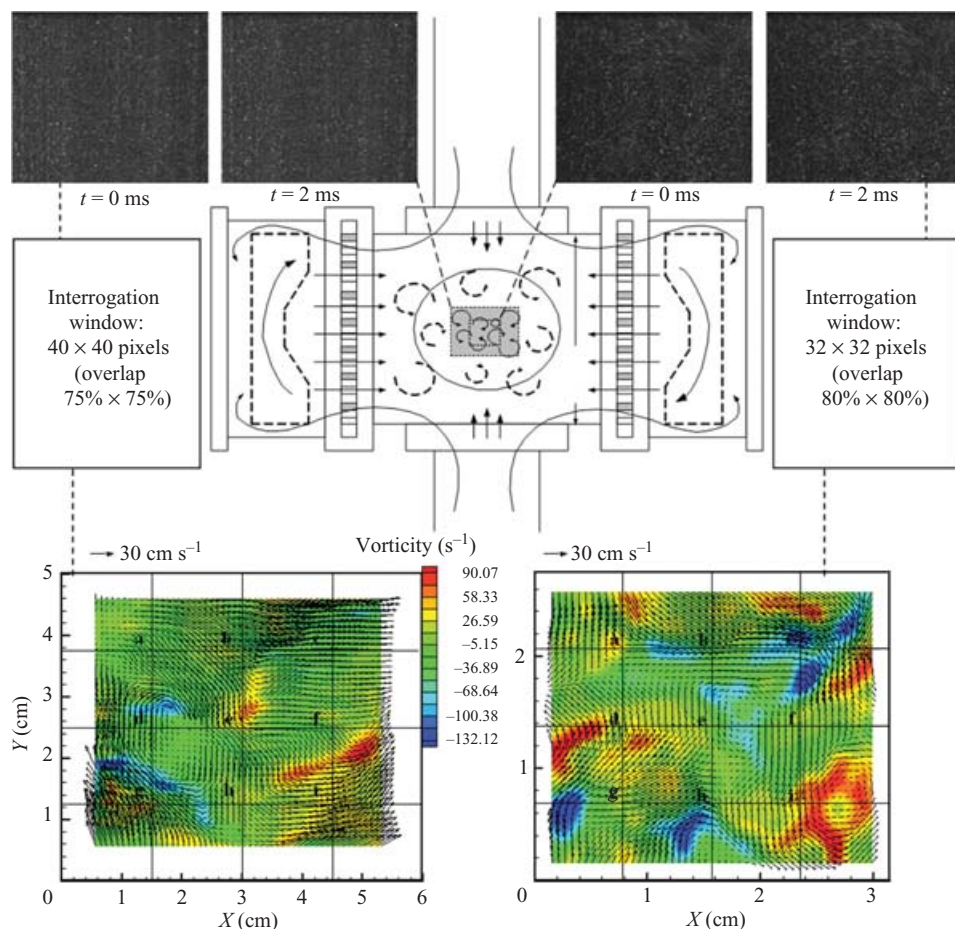
FIGURE 3. A cartoon showing a typical unladen flow pattern at the intersection of the cruciform apparatus. The top four raw images are cross-sectional laser sheet images taken from the near-isotropic region with two different view fields, two images for each with a temporal resolution of 2 ms (500 frames s^{-1}), where $f = 7$ Hz and aluminium powder of 0.3 μm in mean diameter is used for DPIV measurements. Below are two instantaneous velocity maps obtained directly from the above two sets of images, respectively, using DPIV, in which nine points (a–i) equally spaced on the measuring field are selected for temporal analyses using the wavelet transformation. Also plotted are corresponding vorticity maps.

pixels interrogation window on the measuring region, a run begins by performing high-speed DPIV measurements. As a typical example, in the upper right of figure 1, there are three instantaneous, sequential laser sheet images with a field view of 5.84 cm × 5.11 cm (320 × 280 pixels) and with a temporal resolution of 2 ms taken from the central uniform region (figure 3), showing the interaction between heavy particles and near-isotropic turbulence. These images are used for DPIV processing to obtain both velocity and acceleration field maps.

The present cruciform apparatus is a closed system where mean velocities of fluid turbulence are negligible compared to turbulent intensities in the central uniform region, and thus the air mass flux, $\dot{m}_{air}$, is zero. Accordingly, the specific parameter directly related to the modification of fluid turbulence is the volume fraction of heavy

particles rather than the mass loading, $\dot{m}_p/\dot{m}_{\text{air}}$, which cannot be defined in the closed system ($\dot{m}_p$ is the particle mass flux). However, even though the average mass flow rate cannot be defined, it may be possible to infer an average mass loading of about 5% as suggested by referee. Elghobashi & Truesdell (1994) pointed out that for a volume fraction less than 10^{-6}, the presence of particles would have no effect on turbulence; for a volume fraction between 10^{-6} and 10^{-3}, turbulence modification may occur; for a volume fraction greater than 10^{-3}, particle–particle collisions become important and the turbulence of the carrier fluid can be affected by the oscillatory motion due to particle collisions. Thus, in the present study the volume fractions of these three descending heavy particles are kept around 5×10^{-5}. This volume fraction and its corresponding seeding density will keep the out-of-plane loss of pairs small enough that there are about 25–30 particles in a 40×40 pixels interrogated window for accurate DPIV processing, as discussed below.

2.3. *Digital particle image velocimetry and accelerometry*

2.3.1. *DPIV*

The hardware of the DPIV system is schematically shown on figure 1, including a high-power continuous argon-ion laser which is operated at 5 W in this study, the light sheet optics using a combination of cylindrical and spherical lenses to generate a thin laser sheet of 1 mm in thickness, a high-speed CCD camera (Redlake MotionScope PCI 8000 frames s^{-1}) which is operated at either 250 frames s^{-1} with a resolution of 480×420 pixels or 500 frames s^{-1} with a resolution of 320×280 pixels, and a fast personal computer with the PCI card and synchronized circuits. This high-speed DPIV system can provide both spatial and temporal information for unladen and laden turbulent flows. Note that although our laboratory has a 3-D Dantec commercial PIV system using double-pulsed lasers with a pair of high-spatial-resolution (1016×1008 pixels) cameras, its temporal resolution is only $1/30$ s. In order to study the phase coupling mechanism and turbulence modification, a sufficient high temporal resolution that can resolve the time evolution of these intense vorticity structures and particle accumulation clusters in turbulent flow laden with particles is essential. Hence, we make a compromise between the spatial resolution and the temporal resolution by using the high-speed (2 ms or 4 ms) camera with 320×280 pixels or 480×420 pixels, instead of the normal-speed (33.3 ms) camera with 1016×1008 pixels, for investigation of particles settling in turbulence.

The present DPIV system, which is very similar to that developed by Willert & Gharib (1991), uses the double-frame/single-exposure recording technique with cross-correlation analysis based on the fast Fourier transform (FFT). From any two sequential images, the cross-correlation data plane can be obtained by performing the FFT on the images and by a complex-conjugate multiplication of the resulting Fourier coefficients with the inverse Fourier transform. Thus, the displacement from the correlation data at the sub-pixel level can be determined by a three-point estimator using either parabolic or Gaussian peak fits. As the FFT analysis was applied for the correlation calculation, the number of pixels, M and N, respectively expressing the width and height of the interrogation windows, should be a power of 2, e.g. 16, 32, 64, etc. However, the lack of correlation due to small interrogation windows (e.g. 16×16 pixels) may produce erroneous velocity vectors, while with 64×64 pixels one may obtain an overly smooth velocity vector field due to the high degree of averaging in the large interrogation window. Therefore, two improvements are employed in this work. First, we improve the sub-pixel accuracy of the three-point estimator by using spline peak fit, since the commonly used parabolic or Gaussian peak fits are inadequate for

fitting a smooth curve to data points with an asymmetric distribution. The second improvement is to circumvent the restriction of powers of 2 on the interrogation window sizes by applying the technique proposed by Gui & Merzkirch (1998) to generate arbitrarily sized interrogation window sizes for correlation-based analyses of PIV recording. This is essential for the present two-way coupling study, because the motion of heavy particles does not always follow the motion of fluid turbulence due to the phase coupling, and non-uniform particle concentration fields can occur especially when $St \approx 1$ due to the preferential accumulation. Thus, we pad the margins of the arbitrarily sized interrogation window with zeros to meet the restriction of powers of 2 in our Matlab-based FFT software for cross-correlation DPIV processing, so that the effect of the particle density on each interrogation window can be taken into account. It should be noted that velocity estimation using the cross-correlation method over a finite, arbitrarily sized interrogation window has important spatial filtering feature (Saarenrinne & Oiirto 2000 and Sheng, Meng & Fox 2000). Thus, different interrogation window sizes are used, varying from 20×20 pixels to 60×60 pixels for analysing the spatial information contained in these DPIV data. We found that the optimal interrogation window size is 40×40 pixels and is 75% overlapped with the next for DPIV measurements of the present particle-turbulence interaction, as will be discussed in §4.2.

For analyses using arbitrarily sized interrogation windows, a particle volume fraction, c, defined as the ratio of an effective volume occupied by the particles to the total volume of the interrogation window is used. In this study, the laser sheet is about 1 mm thick and has a Gaussian intensity profile. Hence, the heavy particle diameters are much smaller than the laser sheet thickness and particles within the central half of the laser sheet volume contribute most of the incident lights (Raffel, Willert & Kompenhans 1998). The effective volume occupied by the particles is estimated from the total saturated pixels scattered by these particles in a given interrogation window. To remove the background noise and some unwanted signals from particles outside the half of the light sheet thickness, we have carefully selected the appropriate threshold value in the histogram of the grey level from these DPIV images. Thus, variations of the volume fraction of the particles with length (the size of the interrogation window) and time scales can be extracted.

Figure 3 is a cartoon for typical unladen flow patterns in the intersection of the cruciform apparatus with two different pairs of sequential cross-sectional laser sheet images (2 ms) taken from the near-isotropic region for two different view fields shown at the top. Underneath are the two instantaneous fluid velocity maps obtained directly from the above images using DPIV, in which the reference velocity vector arrow of $30\,\text{cm s}^{-1}$ in magnitude is given for comparison, where $f = 7\,\text{Hz}$ and $Re_\lambda = 120$. Also plotted are the corresponding fluid vorticity maps, in which positive and negative values represent counterclockwise and clockwise motions, respectively. As can be seen on figure 3, the highest positive/negative values of vorticity, up to $90\,\text{s}^{-1}/-132\,\text{s}^{-1}$ with red/blue colours, are very rare, revealing that the present flow lacks strong mean shear. There are nine points labelled $(a–i)$ that are equally spaced on the velocity map of figure 3. At these nine points temporal analyses of these velocity maps will be performed using the wavelet-based diagnostic method for both unladen and laden turbulent flows. Each point contains at least 1024 two-component velocity data signals for a recording time of about 2.1 s. For the laden case, the evolution of the particle concentration field, the spatiotemporal responses of heavy particles due to stationary near-isotropic turbulence and turbulence modification due to the particle–fluid coupling can be measured simultaneously.
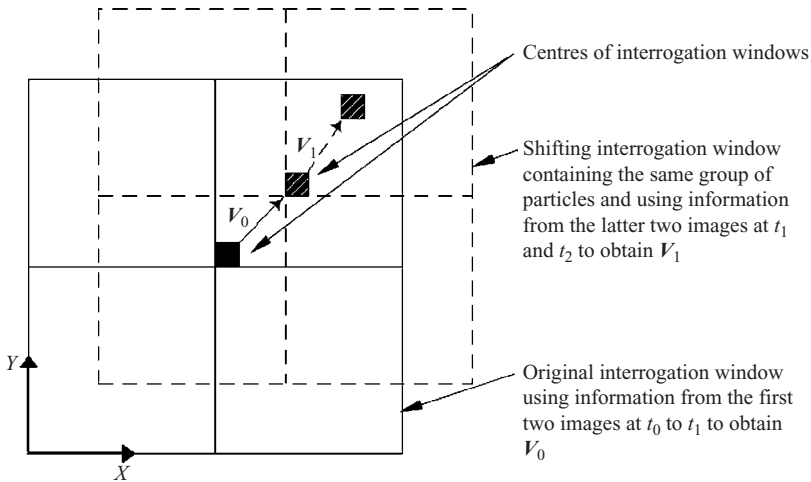
FIGURE 4. A typical diagram illustrating how to calculated the particle Lagrangian acceleration based on an interrogation window shifting concept from three consecutive images at times t_0, t_1 and t_2, where the interrogation window follows the movement of the same group of particles. Thus, the particle Lagrangian acceleration in the original interrogation window can be calculated by $D\boldsymbol{V}/Dt \approx (\boldsymbol{V}_1 - \boldsymbol{V}_0)/(t_1 - t_0)$.

2.3.2. DPIA

It is important to determine the acceleration field in the particle-laden turbulence in order to study the two-way interaction. However, most previous DPIV studies could only resolve the local (Eulerian) acceleration, $\partial \boldsymbol{u}/\partial t$, rather than the full (Lagrangian) acceleration, $D\boldsymbol{u}/Dt = \partial \boldsymbol{u}/\partial t + (\boldsymbol{u}\cdot\nabla)\boldsymbol{u}$, see Chang & Liu (1998), Dong et al. (2001), Jensen et al. (2001), among others. The technique for obtaining the Eulerian accelera- tion is called digital particle image accelerometry (DPIA). Jakobsen, Dewhirst & Greated (1997) were probably the first to obtain the Lagrangian acceleration using DPIV measurements. They used four CCD cameras to measure simultaneously four single-exposure frames (A, B, C, and D) for obtaining two sets of velocity data, respectively from frames A/B and frames C/D, where the time interval between frame B and frame C must be long enough for the estimation of the Lagrangian acceleration. However, whether the fluid parcel can be tracked for a long time interval in a three-dimensional turbulent flow remains unknown. Recently, Christensen & Adrian (2002) applied a two-CCD-camera system with polarization filtering to separate the particle images viewed by each camera, to obtain the instantaneous temporal and convective derivatives of velocity in a channel flow. In this study, we modify the DPIA technique and apply the concept proposed by Christensen & Adrian to measure the acceleration field of heavy particles descending in near-isotropic turbulence using the aforementioned high-speed image acquisition system.

Figure 4 displays a typical diagram to illustrate how to calculate the Lagrangian acceleration based on the image shift concept from three consecutive images at times t_0, t_1, and t_2, respectively. The modified DPIA idea is simple because the DPIV is intrinsically based on the Lagrange specification to track the same fluid parcel or the same group of heavy particles in each interrogation window. As can be seen in figure 4, the velocity $\boldsymbol{V}_0$ of a group of particles in the original interrogation window is obtained using the information from the first two sequential images at t_0 and t_1, which is plotted at the centre of the original interrogation window, marked as a dark

square in the figure. To follow the same group of particles, the original interrogation window is moved with V_0 to the shifted interrogation window (see figure 4), where the information from the later two sequential images at t_1 and t_2 is used to obtain the velocity V_1 that is also plotted at the centre of the shifting interrogation window. Thus, the instantaneous particle Lagrangian acceleration in the original interrogation window can be calculated by

$$\frac{\mathrm{D}V}{\mathrm{D}t} \approx \frac{V_1(X + |V_0|_x \tau, Y + |V_0|_y \tau, t + \tau) - V_0(X, Y, t)}{\tau}, \tag{1}$$

where $|V_0|_x$ and $|V_0|_y$ are the magnitudes of V_0 in the X- and Y-directions, respectively, and $\tau = t_1 - t_0 = t_2 - t_1$. Note that this approach requires a high enough temporal resolution to ensure that nearly the same group of particles in the interrogation window can be tracked at three sequential times. This is achieved when the high-speed CCD camera system is operated at 500 frames s^{-1} with a temporal resolution of 2 ms and the fan frequency is no more than 10 Hz where the maximum fluid velocity is generally much smaller than the energy-weighted r.m.s. turbulent intensity of 30.5 cm s^{-1} (see table 1). For higher fan frequencies ($f > 10$ Hz), the calculation of the particle Lagrangian acceleration using the shifting interrogation window at three sequential times may suffer a larger uncertainty because the autocorrelation of the group of particles between the shifted and original interrogation windows would drop from near 100% to about 70% when f increases from 5 Hz to 12 Hz. This is the main reason why the cutoff fan frequency in this study is 10 Hz, even though the maximum fan frequency in the cruciform apparatus is 172 Hz.

2.3.3. *Estimate of the laden fluid velocity*

In an attempt to measure directly the laden fluid velocity field in the presence of turbulence modification due to the particle–fluid coupling, much effort has been put into using simultaneous two-phase DPIV measurements, seeding with both flow tracer and heavy particles in the present fan-stirred near-isotropic turbulence. After many tests, it is concluded that we are unable to measure the laden fluid velocity in cases where the preferential accumulation phenomenon is significant ($St = 0.36$ and 1.0) with turbulence modification. This is because the clustering heavy particles in these cases block the small tracer particles in that region and make the separation of images useless. Only for the case with sufficiently low particle concentration in which the volume fraction is less than 10^{-6}, can one separate the tracer images from the larger heavy particles. This difficulty was confirmed by Khalitov & Longmire (2002) who used simultaneous two-phase PIV in a turbulent channel flow to measure solids velocities using particle tracking and gas velocities using cross-correlation PIV, with very few solids in the flow field. The presence of these scarce heavy particles would have little influence on fluid turbulence (Ferrante & Elghobashi 2003). Consequently, the preferential accumulation of particle clusters and the two-way coupling effect cannot be studied in this way. Therefore, in order to study the turbulence modification due to the presence of heavy particles, especially when the effect of particle preferential accumulation is significant, an alternative method should be considered. DNS simulations of Wang & Maxey (1993) and Yang & Lei (1998) applied the approximate Basset–Boussinesq–Oseen (BBO) equation to calculate the fluid flow velocity field laden with heavy particles for $\rho_p/\rho_f \gg 1$, and the same approximate BBO equation is used for the present experiment.

For $\rho_p/\rho_f \gg 1$, the BBO equation can be justifiably simplified (Crowe, Sommerfeld & Tsuji 1998) to the form

$$\frac{dV}{dt} = f'(u - V)/\tau_p + g, \tag{2}$$

where V is the instantaneous velocity of a heavy particle at time t, f' is a drag factor, u is the local fluid velocity at the position of the particle, and g is the gravitational acceleration. Here the drag factor $f' = 1 + 0.15\,Re_p^{0.687}$ is used, where $Re_p = |u - V|d_p/\nu$ (see Crowe *et al.* 1998). Using the aforementioned DPIV and modified DPIA techniques, we can obtain the particle velocity field, V, and the particle Lagrangian acceleration field, dV/dt, respectively. Both are then used in equation (2) to calculate the particle-laden fluid velocity, $u = V + (dV/dt - g)\tau_p/[1 + 0.15(|u - V|d_p/\nu)^{0.687}]$, by iteration.

Though in this study only two components of the particle velocity are measured, it should be noted again that the present fan-stirred turbulence has a very high degree of isotropy where turbulent intensities are roughly the same with negligible mean velocities. Therefore, the three-dimensional effect on the particle velocity should be unimportant. In addition, efforts are made to minimize the out-of-plane motion, such setting the cutoff fan frequency to be not greater than 10 Hz and keeping the volume fraction of heavy particles to be around 5×10^{-5}. Nonetheless, this imperfect method using the approximate BBO equation can be used to provide a direct comparison between unladen and laden turbulent flows of turbulent kinetic energy spectra in the frequency domain that enables us to investigate whether the addition of particles would increase or decrease the turbulent kinetic energy of the carrier fluid, as to be discussed in detail. An independent validation of the method is done by measuring simultaneously flow tracer particles (direct measurements) and the heavy particle acceleration field with the approximate BBO equation (indirect measurements) for the case of lead particles with $St \approx 1.9$ where the preferential accumulation is generally absent. It is found that the laden fluid velocity field obtained by the indirect method using the approximate BBO equation combined with DPIV and DPIA techniques is in very good agreement with that measured directly from tracer images, when the distribution of lead particles is uniform in the flow field and the average particle number is greater than 9 in the interrogation window size of $0.63\,\text{cm} \times 0.63\,\text{cm}$ (roughly the size of the Taylor microscale at $f = 7$ Hz). This validation and the detailed description of the phase discrimination of images between discrete lead particles ($d_p \approx 24\,\mu\text{m}$) and aluminium tracer particles ($d_p \approx 0.3\,\mu\text{m}$) are presented in the Appendix.

2.4. *Accuracy of DPIV*

The accuracy of DPIV processing is primarily influenced by four particle image effects, namely the particle image diameter, displacement, density and out-of-plane motion. As noted by Raffel *et al.* (1998), when the particle image diameter is slightly greater than 2 pixels, the r.m.s. uncertainties and fluctuations for typical DPIV cross-correlation calculations are 0.02 pixel and the bias error due to the particle image displacement using the three-point estimator should be negligible. This is the case for the present study. For these DPIV measurements, the particle image densities in both unladen and laden turbulent flows are about 20–30 particles in a 40×40 pixels interrogated window. Since the turbulent velocities in the present study are moderate within the range of about 14–30 cm s^{-1} (see table 1) because of the low fan frequencies ($f = 5$–10 Hz) applied, the corresponding particle image displacements are around 6 pixels

with a r.m.s. uncertainty of about 0.01 pixel using the estimation of Raffel *et al.* (1998). Moreover, the present high-speed DPIV technique has the advantage of very small time intervals between a series of consecutive images because the temporal resolution is selected at 2 ms (500 frames s^{-1}), so that the out-of-plane motion in three-dimensional turbulence can be minimized to a negligible level when $f \leqslant 10$ Hz. The overall particle image error due to the above four effects is about 0.03 pixel and thus the velocity field from these cross-correlation data at the sub-pixel level can be correctly determined.

We have applied various sizes of the interrogation window, namely 16^2, 20^2, 30^2, 32^2, 40^2, 50^2, 60^2, and 64^2 pixels, to test the sensitivity of the spatial resolution to the velocity measurements and to identify the characteristic length scale of preferential particle clusters at different values of the Stokes number, to be discussed later. When the camera is operated at 250 frames s^{-1} with 480×420 pixel resolution on a field of view of 5.84 cm × 5.11 cm, a 16 pixels/interrogation window has a size of about 0.2 cm, about 5η for the $Re_\lambda = 120$ case. It should be noted here that both 16 pixels and 40 pixels/interrogation windows yield essentially the same results on both the size of intense vorticity structures and the length scale of preferential particle clusters, when the cross-correlation algorithm with recursive local-correlation, similar to that developed by Hart (1999), is applied. Using smaller fields of view can further increase the spatial resolution of the velocity measurements. As can be seen on the right-hand side of figure 3 for a field of view 3.14 cm × 2.75 cm, the spatial resolution of a 32 pixels/interrogation window is about 0.3 cm when the camera frame rate of 500 Hz is used. The average sizes of intense vorticity structures over a time period of about 0.5 s are estimated for both cases in figure 3 with different pixel resolutions due to different fields of view, each case having about 250 velocity maps. The result reveals that the sizes of intense vorticity structures are almost the same, ranging from about 0.2–0.5 cm for those values of probability density function (pdf) greater than 0.1 with a pdf peak near 0.4 cm when these two different pixel resolutions are applied (see figure 25 in the Appendix). Moreover, the r.m.s. turbulent intensities obtained from DPIV measurements for the two cases presented in figure 3 are found to be essentially the same within experimental uncertainties ($u' \approx 20$ cm s^{-1} when $f = 7$ Hz). Thus, the present spatial resolution can capture the information on the characteristic length scale of intense vorticity structures of turbulence, when the cross-correlation algorithm with recursive local-correlation is used. Like large-eddy simulation (LES), the velocity fields obtained from PIV measurements are low-pass filtered, in which the corresponding vorticity structures are resolved to finite scales. It should be noted again that small eddies with sizes of a few Kolmogorov length scales have essentially no influence on both the average particle settling velocity and the particle accumulation as pointed out by Yang & Lei (1998) who performed a study on the role of turbulent scales in the particle settling problem using both DNS and LES approaches.

3. Wavelet and intermittency analyses

Farge and coworkers (see Farge 1992) applied the multi-resolution method of wavelet transformations to analyse some elementary structures of turbulence, since the wavelet coefficient in the wavelet domain is the correlation between the corresponding wavelet peaks and valleys from the analysed data signals that may be used to identify the spatial and/or temporal characteristic scales of these signals. In order to study the mechanism that dominates the particle settling behaviour in turbulence, information on the spatiotemporal scales of particle-laden turbulence is required. This is

because the distribution of heavy particles in turbulent flows may exhibit significant intermittency, especially when the spatial and temporal concentration fields of the particles are non-uniform. In order to obtain the essential spatial and temporal scales for the two-way interaction between fluid turbulence and heavy particles, a continuous one-dimensional complex-valued 'Morlet' wavelet is used to transform both unladen and laden velocity data signals obtained by the present DPIV measurements. The wavelet transform coefficient $W(a, b)$ of a continuous real-valued time signal (Farge 1992) can be defined as the inner product between $R(t)$ and an analysed wavelet as

$$W(a, b) = \int_{-\infty}^{\infty} R(t)\phi_{a,b}^*(t)\, dt, \tag{3}$$

where in the present study $R(t)$ can be the velocity time signals in the gravitational or horizontal directions, $w(t)$ or $u(t)$, and/or the particle volume fraction, $c(t)$. In addition, $\phi_{a,b}(t) = (1/\sqrt{a})\phi((t-b)/a)$ with an asterisk superscript to represent its complex conjugate, a and b represent the time dilatation and translation parameters, and the analysed wavelet $\phi_{a,b}(t)$ is a dilated and translated version of a mother wavelet $\phi(t)$ with a resolution of a^{-1} and at a position b (Farge 1992). Note that the complex-valued 'Morlet' wavelet is

$$\phi(t) = \left(e^{i\omega_0 t}\right)\left(e^{-t^2/2}\right), \tag{4}$$

which is used to transform the velocity data signals to obtain $W(a, b)$ that provides not only the strength information about the velocity signals, but also the phase information in both time and scale domains. We use the same admissibility condition for $\phi(t)$ as the one used by Farge (1992),

$$C_\phi = 2\pi \int_{-\infty}^{\infty} \frac{|\hat{\phi}(\omega)|^2}{\omega}\, d\omega < \infty, \tag{5}$$

to ensure the existence of the inverse of the wavelet transform, where $\hat{\phi}(\omega)$ is the Fourier transform of $\phi(t)$. Because the Fourier transform of the Morlet wavelet function is localized around a central frequency ω_c which is equal to ω_o (see equation (4)), we set $\omega_c = \omega_o = 2\pi$ in this study.

As we obtain $W(a, b)$ from equation (3), the effective wavelet energy spectrum in the frequency domain averaged from the nine points (a–i) over the whole flow field (see figure 3) can be defined as

$$E_w(a) = \frac{1}{T} \int_0^T |W(a, b)|^2\, db, \tag{6}$$

where T is the total sampling time of the velocity signals in either the gravitational or the horizontal directions. T is slightly greater than 2 s, so that each of nine points has at least 1024 data samples available for temporal analyses. This wavelet energy spectrum can be used to estimate the energy variation with frequency (the inverse of scale a) for both unladen and laden turbulent flows, analogous to the Fourier energy spectrum (Bonnet *et al.* 1998). Moreover, the wavelet coefficient $W(a, b)$ that represents the variation of the velocity signals at a given scale and at a given time can be used to investigate the issue of intermittency, a crucial aspect of turbulence, based on the flatness factor F (see Camussi & Guj 1997 and Mouri *et al.* 1999, among others). Here F of the 'Morlet' wavelet coefficient used in this study for both unladen and laden turbulent flows is

$$F \equiv \langle |W(a, b)|^4 \rangle_t / \langle |W(a, b)|^2 \rangle_t^2, \tag{7}$$

where the subscript t represents the temporal analysis. This F is equivalent to the fourth order of the velocity structure function: $F = \langle |\Delta V(r)|^4 \rangle / \langle |\Delta V(r)|^2 \rangle^2$ where ΔV is the velocity increment between two velocity signals at a time separation r. Equation (7) is used to evaluate the level of intermittency of the present turbulent flow with and without heavy particles. Note that the higher the value of F, the higher the level of intermittency (Camussi & Guj 1997). Concerning the spatial wavelet analysis of these velocity data signals, the corresponding wavelet equations are essentially the same as those for the temporal analysis except that time is replaced by a length scale measured by the distance between two points on the velocity map at a fixed Y position along the X direction (see figure 3). In this work, we select three different Y positions, $Y = 1.25$ cm, 2.50 cm, and 3.75 cm (see figure 3) for spatial wavelet analyses. Thus, the corresponding flatness factor F as a function of the length scale for both horizontal and vertical components at a fixed Y on the velocity map along the X direction can be determined. From both spatial and temporal analyses of the flatness factor, not only can the level of intermittency between unladen and laden turbulent flows be identified and compared, but also the characteristic length and time scales responsible for the preferentially accumulated particle clusters can be justified when the particle volume fraction $c(t)$ is used to replace the velocity time signals $R(t)$ in equation (3).

4. Results and discussion

In an attempt to provide a full assessment of the particle settling behaviour in turbulence, three general issues were investigated experimentally, namely (i) the long-time particle concentration field, (ii) the mean settling rate for heavy particles in the gravitational direction, and (iii) the particle–fluid two-way coupling. It should be noted that the present experiment may be representative of the 'equilibrium' state of a turbulent field laden with particles, because the time spend by the particles in the region of interest (~ 10 cm) is about $100\tau_k$ and this long residence time, according to Wang & Maxey (1993), is sufficient to observe the asymptotic behaviour of the settling velocity and to avoid the transient associated with the formation of clusters. In this section, we shall begin with a short description of fluid turbulence, particularly the spatiotemporal intermittency, and then discuss the above three issues in detail.

4.1. *Unladen fluid turbulence*

Figure 5 shows four instantaneous velocity maps superimposed on the corresponding vorticity maps using DPIV for the case of $f = 7$ Hz where $Re_\lambda = 120$ with the temporal resolution of 2 ms. The intense vorticity structures with highest positive/negative values of vorticity, as indicated by the colour bar on figure 5, are rare in the whole flow map at any instant. Moreover, these intense vorticity structures appear in roughly circular regions, closely matching tube-like vortical structures, where the corresponding velocity gradients are more significant. The average diameter or width of these tube-like structures is around 0.2–0.5 cm, about 5–12.5 Kolmogorov length scales, in support of DNS data found by Jiménez *et al.* (1993). Concerning the wavelet spectrum using equation (6), figure 6 displays typical average wavelet energy spectra obtained from the evolution of these velocity data at the nine points (a–i) equally spaced over the measurement flow field in the central uniform region (see figure 3), including both horizontal (u) and vertical (w) velocity components for the case of $f = 7$ Hz where $Re_\lambda = 120$. As can be seen from figure 6, the inertial range of $-5/3$ slope can span a wide spectrum from 3 Hz to 200 Hz for both vertical and horizontal
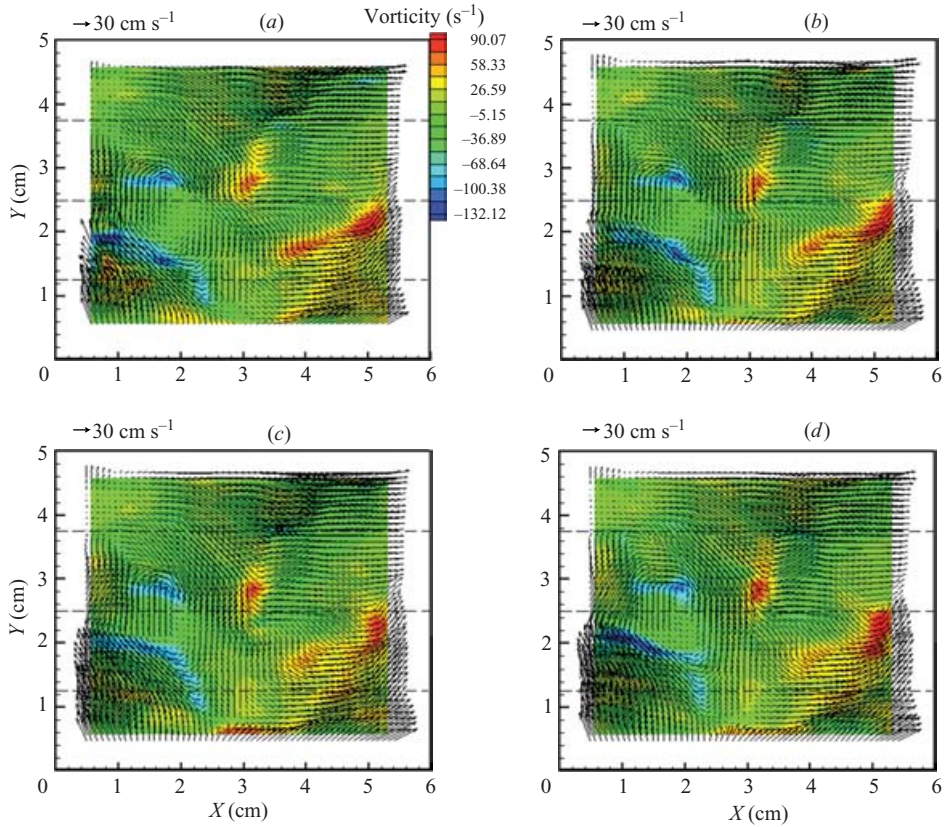
FIGURE 5. Four instantaneous velocity maps superimposed on the corresponding vorticity maps using DPIV for the case of fan-stirred near-isotropic turbulence at $f = 7\,\mathrm{Hz}$ where $Re_\lambda = 120$ based on the Taylor microscale at (a) $t = 0.002\,\mathrm{s}$, (b) $t = 0.004\,\mathrm{s}$, (c) $t = 0.006\,\mathrm{s}$, (d) $t = 0.008\,\mathrm{s}$. Three lines at different Y positions along the X direction as indicated by the dashed lines are selected for spatial analysis using the wavelet transformation.

components. Other spectra at different locations of the flow or in different cases with $Re_\lambda = 73$ and 202 (not shown) all reveal a wide inertial range with a slope of $-5/3$. It deserves comment that the average wavelet energy spectra in both horizontal and vertical directions are very close to each other around the integral time scale, revealing that the r.m.s. velocity fluctuations in these two directions are nearly the same with negligible mean velocities. Thus, the present fan-stirred turbulent flow has properties similar to that of fully developed turbulence with a high degree of isotropy.

It is known that values of the wavelet coefficient at different scales can give quantitative information on the level of intermittency, which characterizes some of the flow statistical mechanics of turbulence, see Farge *et al.* (1996). Thus, the wavelet-based calculation of the flatness factor selected from the wavelet coefficient at different scales acts as a quantitative indicator of the level of intermittency in the analysed turbulent flow. When a Gaussian probability distribution of the velocity signals is considered, $F = 3$. The higher the value of F is, the higher the level of intermittency of the fluid turbulence. Figures 7(a) and 7(b) respectively present the distribution of values of F in the frequency and the length scale domains, each including both components of velocity signals at $Re_\lambda \approx 120$. For the temporal analysis, values of F
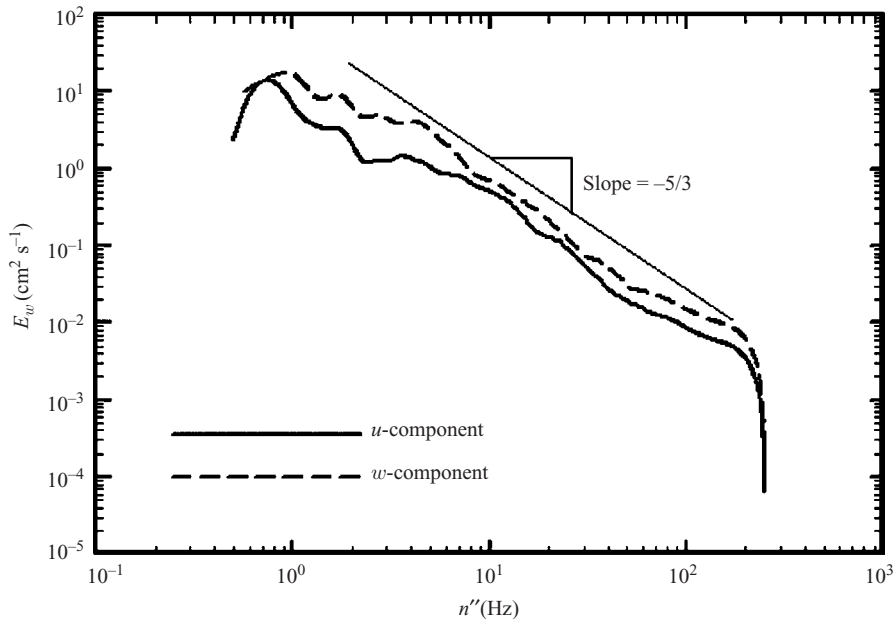
FIGURE 6. The average wavelet frequency spectra of the present fan-stirred near-isotropic turbulence in both horizontal and vertical directions, where the experimental conditions are the same as in figure 3.

are nearly 3 within the range of about 8–24 Hz, closely matching the integral time scale and the Taylor microscale of the inertial range, respectively (see figure 7a). As the characteristic frequency n'' increases, values of F continue to increase and then reach a maximum of about 10 around $n'' \approx 110$ Hz in the present near-isotropic turbulence. This specific frequency is approximately the inverse of the Kolmogorov time scale of fluid turbulence, as represented by the dashed arrow in figure 7(a). In short, the highest value of F, equivalent to the highest level of intermittency due to the intermittent scale of the small intense vorticity structure of turbulence, occurs around the Kolmogorov time scale.

Concerning the spatial analysis, figure 7(b) shows typical variations of values of F with the separation length at three different Y positions along the X direction for both horizontal (u) and vertical (w) velocity components, namely at $Y = 1.25$ cm, 2.50 cm, and 3.75 cm (see figure 3). Values of F start to increase slowly as the characteristic length scale decreases from about 4 cm (see figure 7b from right to left). Then the length scale dependence of F becomes much stronger when the length scale is less than the Taylor microscale (~ 0.86 cm). Finally, values of F reach their maximum when the length scale is further decreased to within the range 0.2–0.5 cm, equivalent to 5–12.5 Kolmogorov length scales, as shown on figure 7(b). That length scale range where the F has its maximum value may be viewed as the footprint of the most intermittent vortical structures of fluid turbulence. This can be also seen at $Y = 1.25$ cm along the X direction on the vorticity map of figure 3, where small-scale intense vorticity structures are obvious and have roughly an average size of 5η–12.5η that corresponds to the most intermittent level of turbulence (highest values of F), consistent with the F results presented in figure 7(b). Furthermore, these spatial F results at different Y for both horizontal and vertical components all reveal the
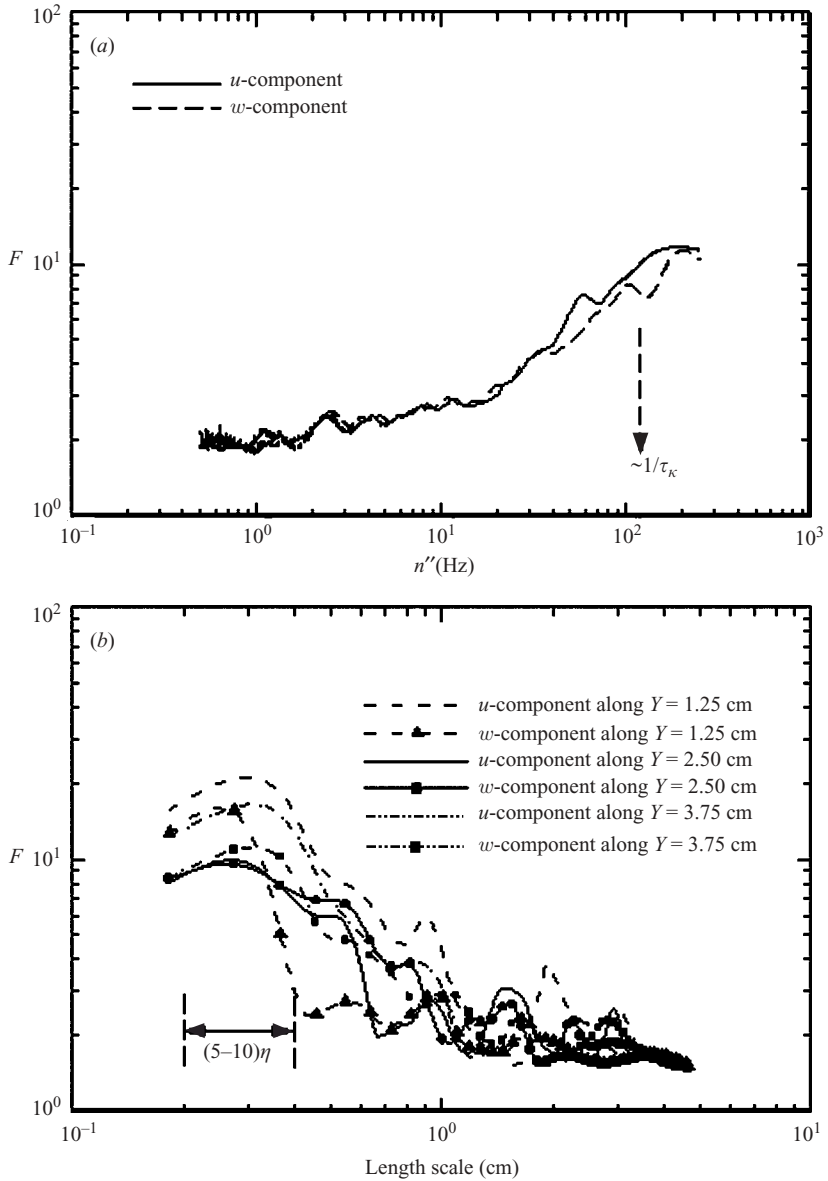
FIGURE 7. (*a*) The flatness factor F as a function of the frequency for temporal wavelet analyses, where the F data are averaged from nine data sets corresponding to nine points $(a–i)$ on figure 3, each data set having 1024 samples. (*b*) Similar to (*a*), but plotted against the separation distance between two points on the velocity map along the X direction, including both horizontal and vertical components at three different Y positions illustrated on figure 5, where $f = 7\,\mathrm{Hz}$ and $Re_\lambda \approx 120$.

same trend, indicating that this flow has a high degree of homogeneity. Hence, the characteristic length scale of most intermittent vorticity structures of turbulence in the dissipation range is not the commonly assumed Kolmogorov length scale, but is approximately an order of magnitude greater than η.

4.2. *Preferential accumulation of particle clusters*

4.2.1. *The evolution and the build-up time of particle clusters*

Figures 8 to 10 present the time evolution of three different heavy particles interacting with turbulence at a fixed $Re_\lambda = 120$, namely copper particles of $d_p \approx 12\,\mu m$ with $St \approx 0.36$, glass particles of $d_p \approx 40\,\mu m$ with $St \approx 1.0$, and lead particles of $d_p \approx 24\,\mu m$ with $St \approx 1.9$. See table 2 for these particles' properties. Each of these three figures includes ten consecutive images taken from the near-isotropic region with a field of view 5.84 cm × 5.11 cm and at a time interval of 4 ms. At $St \approx 0.36$ as well as at $St \approx 1.0$, the concentration fields are quite non-uniform, because regions of either near-zero or significant accumulation can be clearly seen on figures 8 and 9, respectively. On the other hand, in the case of $St \approx 1.9$ (figure 10), the particle concentration field has more or less a random distribution and no particle accumulation is observed. These observations reveal three points. (i) The so-called preferential accumulation due to the inertial bias when $St \sim 1.0$ (see Wang & Maxey 1993; Fessler & Eaton 1999, among others) is confirmed in the present fan-stirred near-isotropic turbulence. (ii) These clustered particles in figures 8 and 9 form structures somewhat like 'sheets' that distribute themselves along the periphery of intense vorticity eddies. (iii) The time required for the formation of these clusters is of the order of the Kolmogorov time scale (τ_k). This latter point is found from the comparison between the characteristic eddy turnover time of $\lambda/u' \approx \sqrt{15}\tau_k \approx 40\,$ms and the temporal evolution of the particle concentration field for which the total sampling time of these ten consecutive images is 36 ms, as will be further discussed. Taking the image at $t = 28\,$ms in figure 8 as a typical example, the preferential accumulation is clearly seen in the lower half of the image and significant clusters of particles are organized as sheet-like structures located near the adjacent boundaries among these intense vorticity structures.

For the build-up time of the clusters, the present data gives about $4\tau_k$ which is significantly shorter than that reported by Wang & Maxey ($\sim 20\tau_k$–$30\tau_k$). This difference is probably due to different initial conditions of given particles in turbulence. According to Wang & Maxey (1993) when using the triplex averaging procedure, particles were assumed to be located randomly with a uniform distribution in a statistical stationary flow velocity field, and the initial velocity for each descending heavy particle was assumed to be the particle terminal velocity. Therefore, the temporal evolution of the particle concentration field starting with a random distribution, intuitively, may be divided into three stages before reaching the stationary state. Namely, (i) the inertial adjustment of the particles in the flow velocity field, (ii) the rapid change of the particles responding efficiently to the dynamics of the flow structures, and (iii) the final asymptotic stage in which there exists a balance between the preferential accumulation due to local vortical structures and random stirring at large scales. Hence, the built-up time of the clusters, t, was larger than $2T_e$, equivalent to $20\tau_k$–$30\tau_k$, where T_e ($\equiv u'^2/\varepsilon$) was the eddy turnover time (Wang & Maxey 1993). Note that after reaching the final asymptotic a stage small final adjustment in the concentration distribution is likely even for $t > 2T_e$. The triplex averaging procedure was also employed by Yang & Lei (1998) for the particle calculation. They found that if the initial velocity of a given particle was set equal to the particle terminal velocity plus the local fluid velocity, the time scale required for the formation of particle clusters was on the order of $\lambda/u' \approx \sqrt{15}\tau_k$ which was related to the mean enstropy of the flow field (Yang & Lei 1998). The present finding reveals that the characteristic built-up time associated with the clusters is about $4\tau_k$, in support of the Yang & Lei's numerical result.
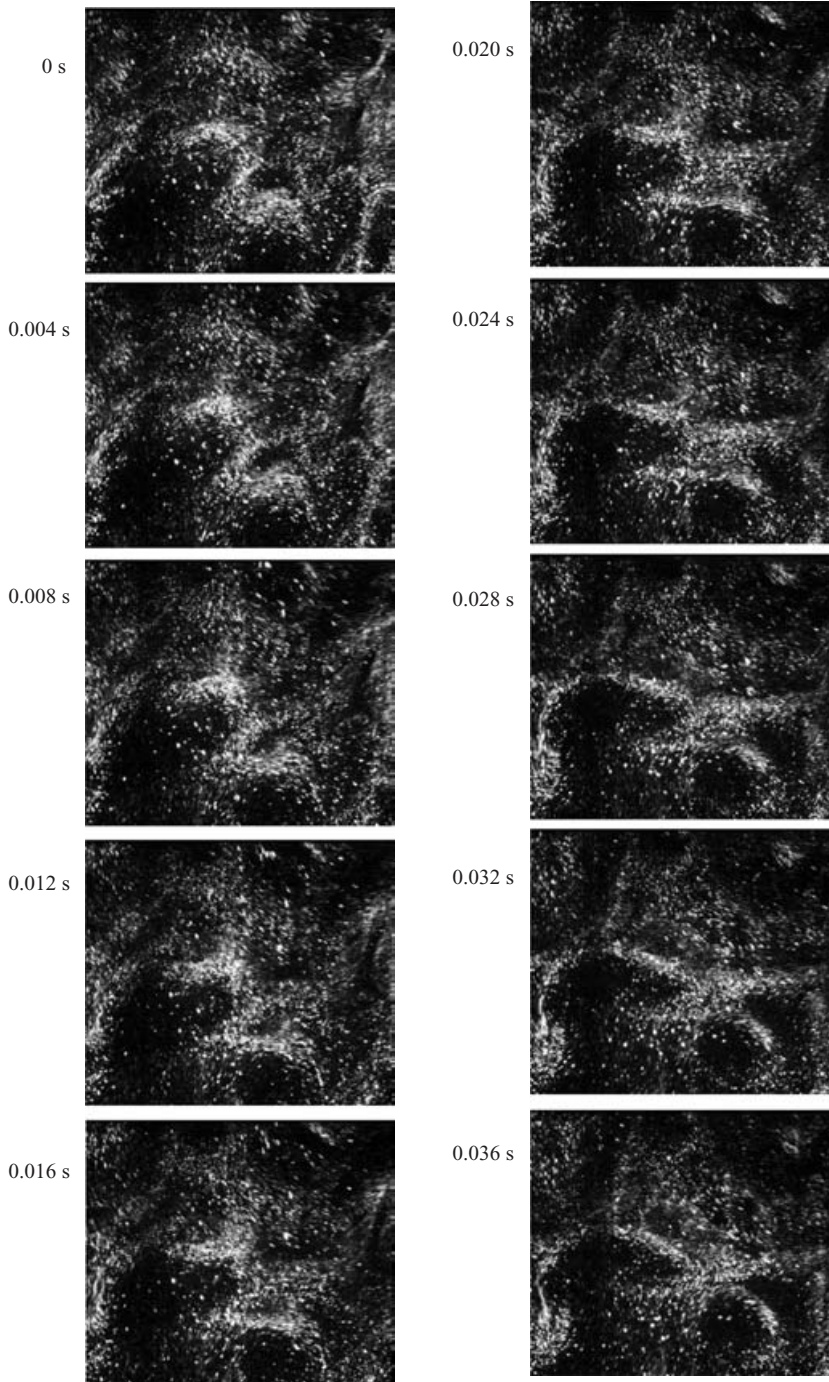
FIGURE 8. The time evolution of heavy copper particles interacting with near-isotropic turbulence where the experimental conditions are $f = 7\,\text{Hz}$, $Re_\lambda \approx 120$, and $St \approx 0.36$. The time origin is selected as when the stationary near-isotropic turbulence has already been established and the DPIV acquisition is just begun.
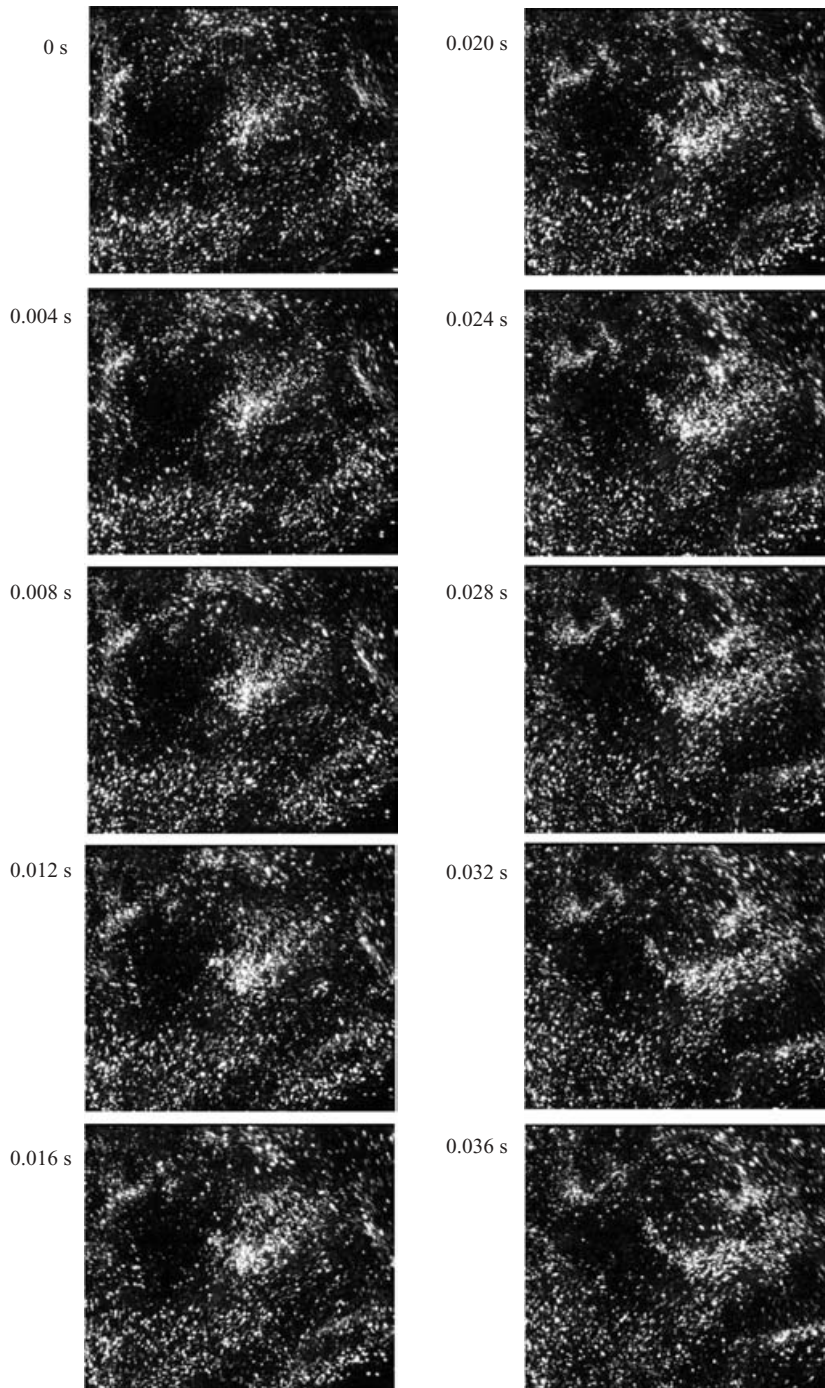
FIGURE 9. Same as figure 8, but for glass particles of $d_p \approx 40\,\mu\text{m}$ where $St \approx 1.0$.

4.2.2. *The spatiotemporal information and the effect of cell sizes*

We employ arbitrarily sized interrogation windows on each of digitized images (see §2.3.1) and apply analyses of the flatness factor using the wavelet transformation (see
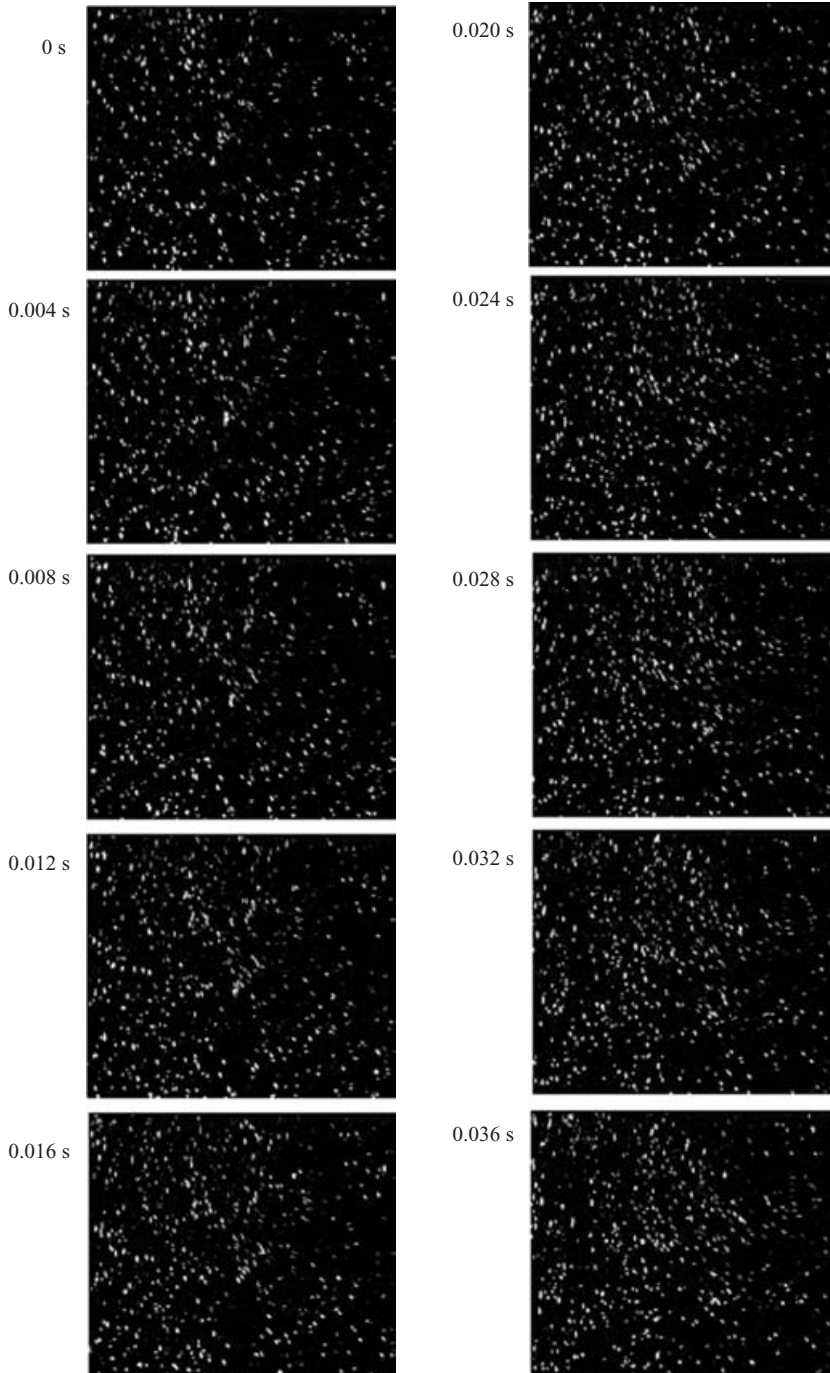
FIGURE 10. Same as figure 8, but for lead particles of $d_p \approx 24\,\mu$m where $St \approx 1.9$.

§3) to further quantify the spatiotemporal information on these three heavy particle concentration fields. Figure 11(a) presents the temporal result of the flatness factor of the volume fraction averaged from points (a–i) on figure 3 using an interrogation window of 40×40 pixels for three different particles that correspond to Stokes
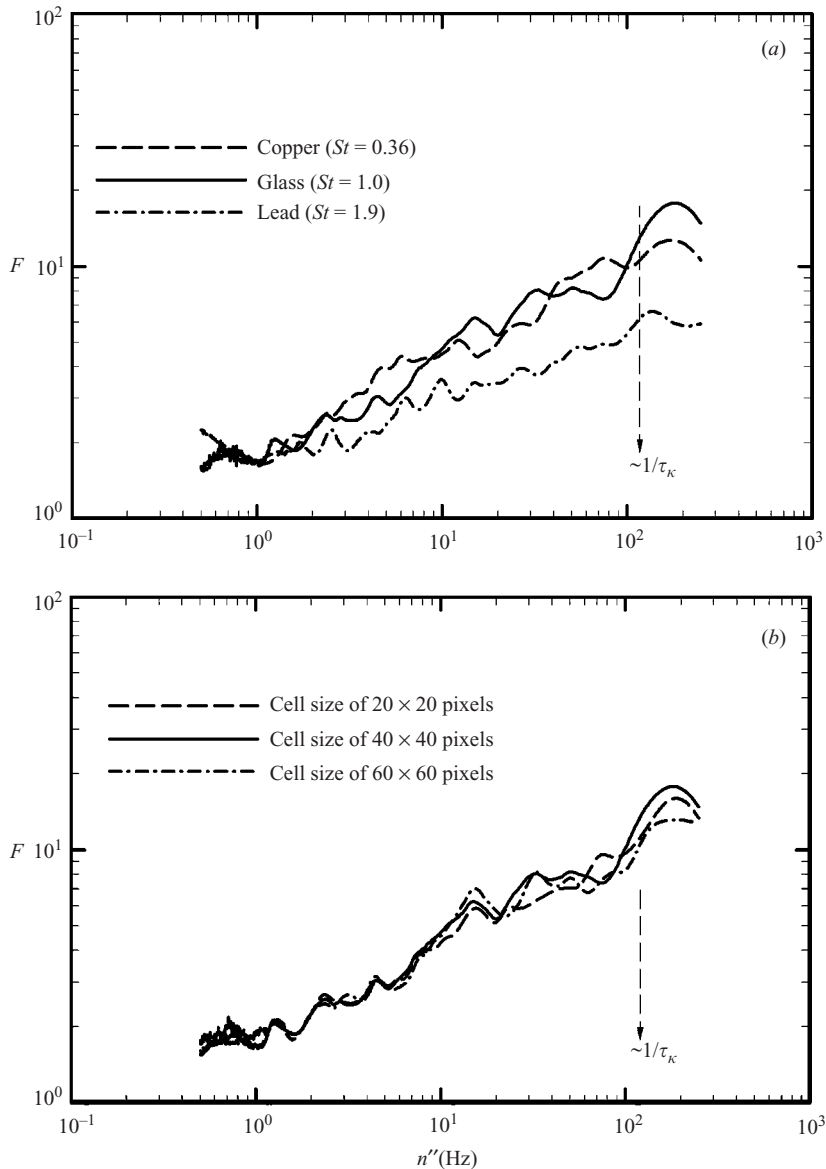
FIGURE 11. The flatness factor F of the volume fraction as a function of the frequency for temporal analysis. (*a*) F for different Stokes number at a fixed cell size of 40×40 pixels. (*b*) Effect of the cell size on the variation of the volume fraction for glass particles for which $St \approx 1$.

numbers $St \approx 0.36$ (figure 8), $St \approx 1.0$ (figure 9) and $St \approx 1.9$ (figure 10), respectively. Also plotted is the inverse of the Kolmogorov time scale of turbulence at $Re_\lambda = 120$ to indicate the characteristic frequency in the dissipation range. As can be seen from figure 11(*a*), values of F reach their maximum when the frequency scale n'' increases up to or slightly beyond τ_k^{-1}, revealing that the most significant temporal intermittency of these heavy particle concentrations occurs around τ_k. In other words, the Kolmogorov time scale of fluid turbulence dominates the characteristic temporal
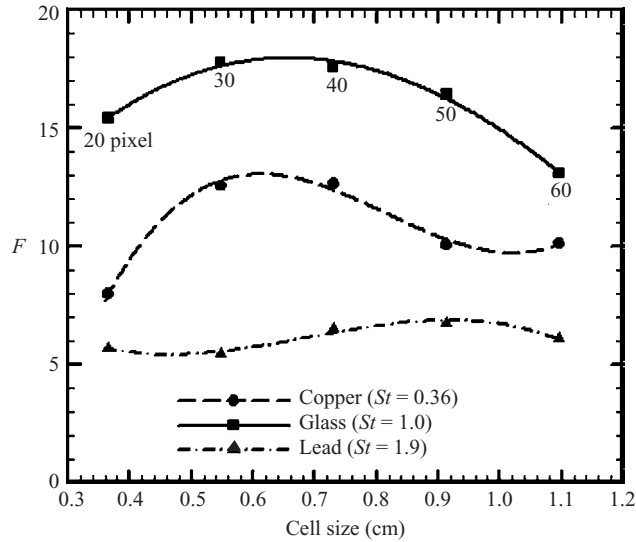
FIGURE 12. The conditional averaging of F for the volume fraction of three descending heavy particles sampled around the Kolmogorov time as a function of cell size, where $f = 7\,\mathrm{Hz}$ and $Re_\lambda \approx 120$.

passage of these particle clusters, independent of St. However, the parameter St plays an important role in the degree of particle preferential accumulation, because the most significant accumulation occurs at $St \approx 1.0$ at which the maximum F is as high as 18, while the maximum F is only about 6.5 when $St \approx 1.9$ where essentially no accumulation is observed (see figures 11a, 9, and 10).

The effect of different cell sizes on the flatness factor of the volume fraction for glass particles with $St \approx 1$ is displayed on figure 11(b). Though the increasing trend of the value of F with increasing n'' and the characteristic frequency around τ_k^{-1} for the occurrence of the most significant intermittency of these particle concentration fields are essentially the same among these three different cell sizes, it is found that the appropriate interrogation window size is around 40×40 pixels in order to capture the most significant intermittency of the particle concentration field. The cell size of 40 pixels is 0.72 cm, which is very close to the Taylor microscale of $\lambda = 0.86$ cm when $Re_\lambda = 120$ and approximately equivalent to the characteristic length scale of particle clusters shown on figure 9.

Following the same process as in figure 11, a conditional average of F of the volume fraction for the three descending heavy particles, which is sampled around τ_k^{-1} at which F is maximum, is plotted against the cell size to identify the characteristic length scale of these particle accumulation regions at different values of St, as shown on figure 12. It can be seen again that the highest value of the maximum F for either $St \approx 1.0$ or $St \approx 0.36$ occurs near the interrogation cell size of about 40 pixels, closely matching the Taylor microscale. The most significant particle preferential accumulation occurs at $St \approx 1.0$ where the value of the maximum F is highest among these three values of St for all cell sizes studied. On the other hand, essentially no particle preferential accumulation is observed in the case of $St \approx 1.9$, where the laden turbulent flow has rather weak intermittency for which the maximum F is only about 6.5. This preferential accumulation scenario can be also demonstrated by the probability density function distribution of the normalized particle volume fraction
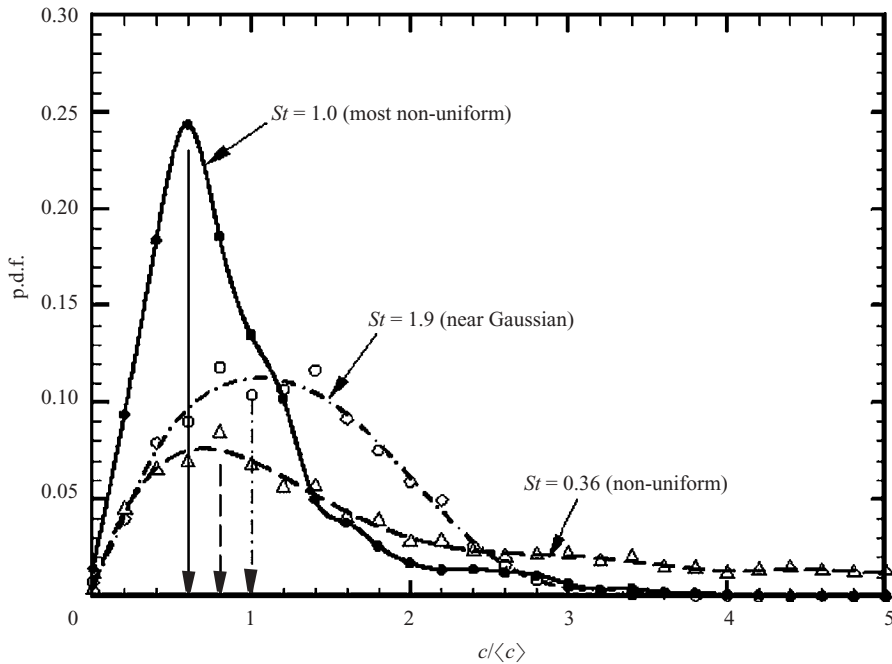
FIGURE 13. The probability distribution of the normalized particle volume concentration, $c/\langle c \rangle$, for three descending heavy particles of different Stokes number, where $f = 7\,\text{Hz}$ and $Re_\lambda \approx 120$.

for these three cases with different values of St, where $\langle c \rangle$ is the mean volume fraction averaged over the whole flow field using the interrogation window of 40×40 pixels, see figure 13. The p.d.f. distribution for the case of $St \approx 1.9$ is quite close to a Gaussian shape with the peak around $c/\langle c \rangle = 1$, revealing that the particle concentration field is rather randomly distributed without the preferential accumulation. On the other hand, the particle concentration field is most non-uniform in the case of $St \approx 1$, where the peak p.d.f. occurs at $c/\langle c \rangle = 0.6$, indicating that these lower-concentration regions occupy a major fraction of the whole flow field. This is equivalent to saying that a noticeable amount of heavy particles accumulates at some specific locations of the flow field, as can be clearly seen on figure 9.

These results show that the most significant preferential accumulation due to the inertial bias occurs near $St = 1.0$. The characteristic length scale of these particle clusters that distribute themselves around the periphery of intense vortical structures is of the order of the Taylor microscale, and the characteristic temporal passage of these particle clusters is of the order Kolmogorov time scale.

4.3. *Mean particle settling velocity*

The present high-speed DPIV measurement is operated at a time rate of 500 frames s^{-1} for about 2.1 s, slightly more than 8.5 integral time scales, so that there are at least 1024 instantaneous particle velocity maps in a run available for spatiotemporal analyses. Figure 14 shows two typical instantaneous particle velocity maps superimposed on their corresponding instantaneous particle concentration distributions at a constant turbulent Reynolds number $Re_t = 362$ or $Re_\lambda = 120$ ($f = 7\,\text{Hz}$; see table 1), for (*a*) copper particles where $St \approx 0.36$ and (*b*) glass particles where $St \approx 1.0$. For the
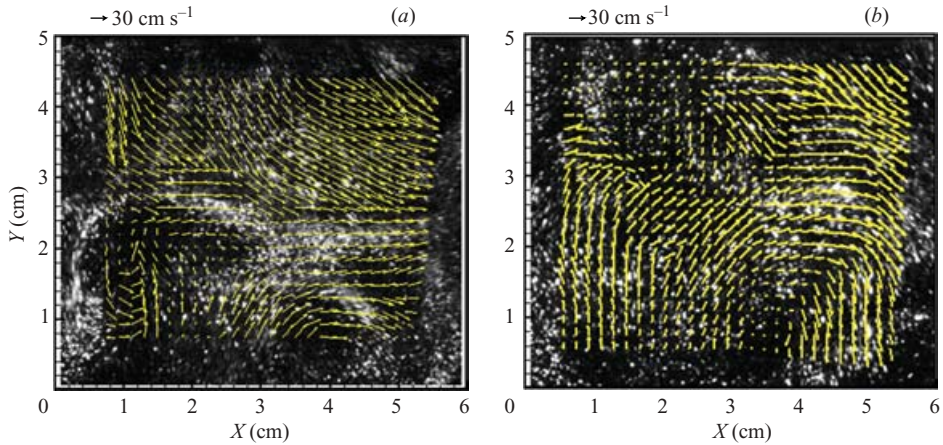
FIGURE 14. The instantaneous particle velocity map superimposed on the corresponding particle concentration field at a fixed $Re_\lambda \approx 120$ for (*a*) copper particles and (*b*) glass particles.

present study in the case of preferential accumulation where local concentrations occur, 99.7% of the particle velocity field is valid when the large interrogation window of 40×40 pixels is used. Only 0.3% of the velocity measurements have significant uncertainty because of very small particle numbers, and this rather small bias may be neglected. We average all available particle velocity data from these 1024 instantaneous particle velocity maps to obtain an ensemble-average particle settling velocity, V_s. Figure 15 shows the mean particle settling rate, $(V_s - V_t)/V_t$, as a function of St for glass particles with $d_p \approx 40\,\mu\text{m}$ at three different fan frequencies, $f = 5, 7$, and $10\,\text{Hz}$, corresponding to $Re_\lambda = 73, 120$, and 202, where the corresponding values of V_t/v_k and V_t/u' are 3.5 and 0.80, 3.0 and 0.55, and 2.7 and 0.37, respectively. The vertical and horizontal error bars on these three data points for glass particles represent the standard deviation of V_s measurements from several identical runs and the possible range of St due to the variation of d_p between $34\,\mu\text{m}$ and $43\,\mu\text{m}$ for glass particles, respectively. In addition, figure 15 includes two more results obtained at $Re_\lambda = 120$ ($f = 7\,\text{Hz}$) using copper particles of $d_p \approx 12\,\mu\text{m}$ where $V_t/v_k \approx 1$ and $V_t/u' = 0.2$ and tungsten particles of $d_p \approx 24\,\mu\text{m}$ where $V_t/v_k \approx 5$ and $V_t/u' \approx 0.95$, respectively. Also plotted are previous numerical results of figure 16 from Yang & Lei (1998) where the data of $V_t/v_k = 3$ at both $Re_\lambda = 65$ and 133 are selected for comparison. Data from other studies cannot be directly plotted for comparison (see figure 12 of Friedman & Katz 2002). As can be seen from both experimental and numerical data, the relative variation of the mean particle settling rate for $Re_p < 1$ due to turbulence may be characterized by three dimensionless parameters, $St = \tau_p/\tau_k$, V_t/v_k or V_t/u' and Re_λ. When $St \sim 1$ and $V_t/v_k \sim 3$, the glass particle data reveal that values of $(V_s - V_t)/V_t$ increase significantly from 13% to 38% when Re_λ increases from 73 to 202, indicating a strong Re_λ influence on the mean settling rate. This dependence on Re_λ is consistent with previous numerical results by Yang & Lei (1998) for about the same Re_λ.

The plot of $(V_s - V_t)/V_t$ versus St as presented in figure 15 is not a good presentation to reveal the influence of small-scale turbulence on particle settling velocities, because the settling rate is not only influenced by St but also by V_t/v_k and/or V_t/u'. Thus, we re-plot these experimental data points at $Re_\lambda = 120$ from figure 15 on figures 16(*a*) and 16(*b*), where the ordinate, the mean settling rate, is changed to $(V_s - V_t)/u'$ and both

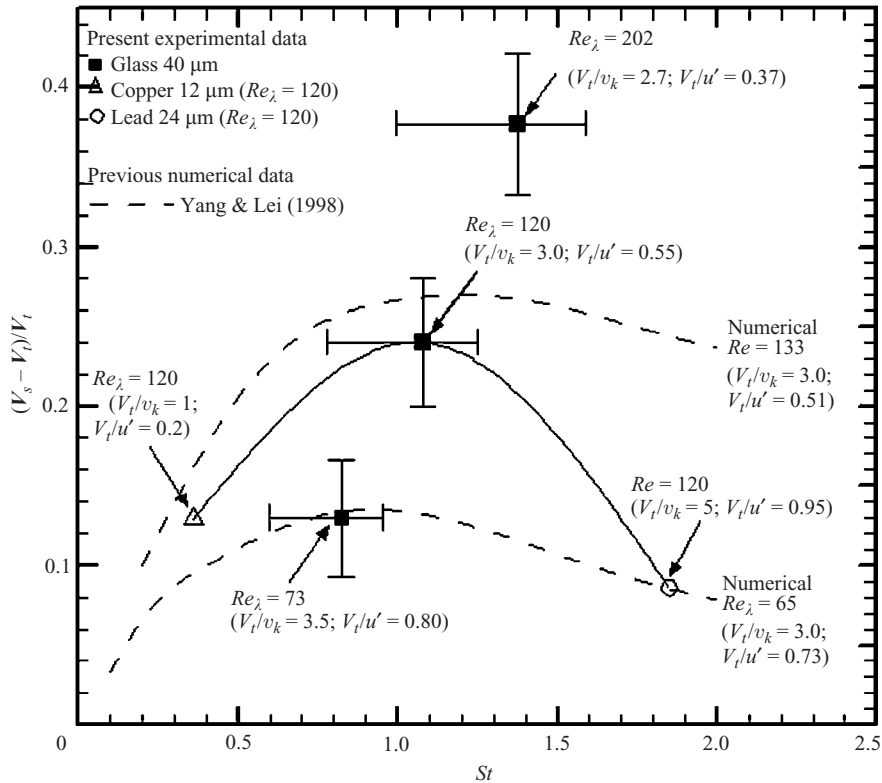FIGURE 15. Effect of the Stokes number and the Taylor Reynolds number on the settling rate, $(V_s - V_t)/V_t$. Also plotted are numerical results from Yang & Lei (1998) for comparison.

St and V_t/v_k or V_t/u' are used as the abscissa, respectively. Note that all experimental and numerical data presented on figure 16 have the same values of $St/(V_t/v_k) = 0.36$ in (a) and $St/(V_t/u') = 1.96$ in (b), respectively, so that a direct comparison between these two different approaches can be made. Figure 16 shows that the maximum settling rate, $(V_s - V_t)/u'$, occurs when St is of the order of unity where $V_t/v_k \approx 3$ in (a) and $V_t/u' \approx 0.5$ in (b) for both experimental and numerical results. Hence, it is confirmed that the Kolmogorov time scale of turbulence has the strongest influence on the mean particle settling rate because $(V_s - V_t)/u'$ is maximum of 0.13 when $St = \tau_p/\tau_k \approx 1$. Furthermore, a much better agreement between experimental and numerical results is found for the constant-$St/(V_t/u')$ data, as shown on figure 16(b). This suggests that the turbulent velocity scale which dominates the settling may be the characteristic turbulent intensity, u', rather than the Kolmogorov velocity scale, v_k. The other two cases in figure 15 (glass particles) with St near unity at different Taylor's Reynolds numbers $Re_\lambda = 73$ and 202 reveal the same result. In short, the settling phenomenon is strongly influenced by intense vorticity structures in which the time and velocity scales that dominate the mean settling rate may be τ_k and u', respectively.

4.4. *Particle Lagrangian acceleration and laden fluid velocity fields*

Figures 17(a) and 17(b) present the instantaneous particle Lagrangian acceleration fields superimposed on their corresponding particle concentration distributions for copper particles and glass particles, respectively, using the Lagrangian interrogation window concept (see figure 4) on the data of figure 14. Thus, the instantaneous
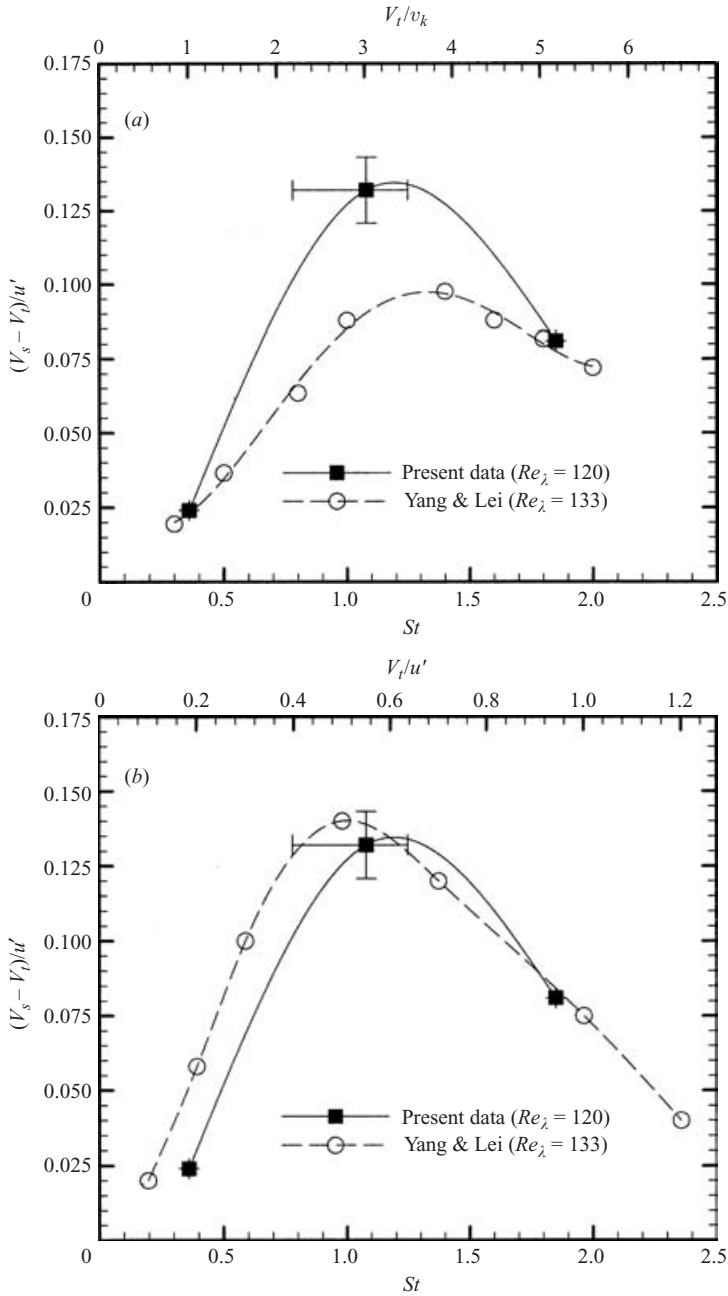
FIGURE 16. The normalized mean settling rate, $(V_s - V_t)/u'$, plotted against St and (a) V_t/v_k and (b) V_t/u' at $Re_\lambda \approx 120$ ($f = 7$ Hz), where numerical data extracted from figure 16 of Yang & Lei (1998) are also plotted for comparison. Both experimental and numerical data have the same values of (a) $St/(V_t/v_k) = 0.36$ and (b) $St/(V_t/u') = 1.96$.

particle-laden fluid velocity fields and their corresponding vorticity fields can be obtained by using these data of V (figure 14) and dV/dt (figure 17a, b) in the BBO equation. The result is presented in figures 17(c) and 17(d) for copper and glass
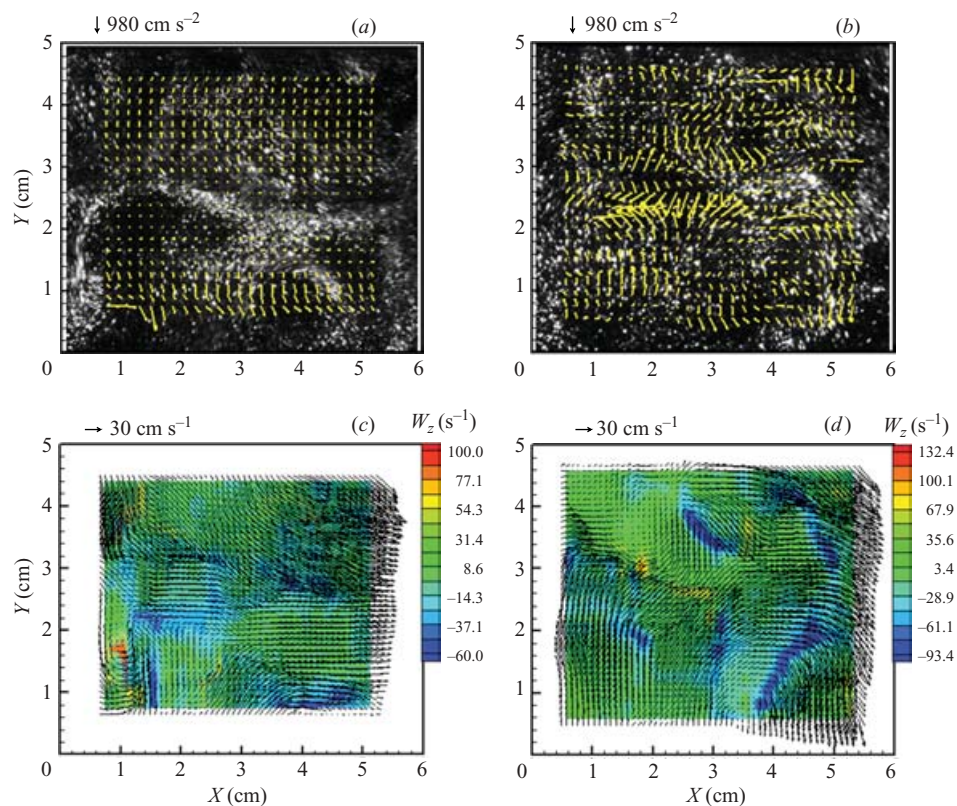
FIGURE 17. Similar to figure 14, but for the particle Lagrangian acceleration fields: (*a*) copper particles ($St = 0.36$) and (*b*) glass particles ($St = 1.0$). (*c*) The particle-laden flow velocity field superimposed on its corresponding vorticity field in the presence of copper particles. (*d*) Same as (*c*), but for glass particles. $Re_\lambda = 120$.
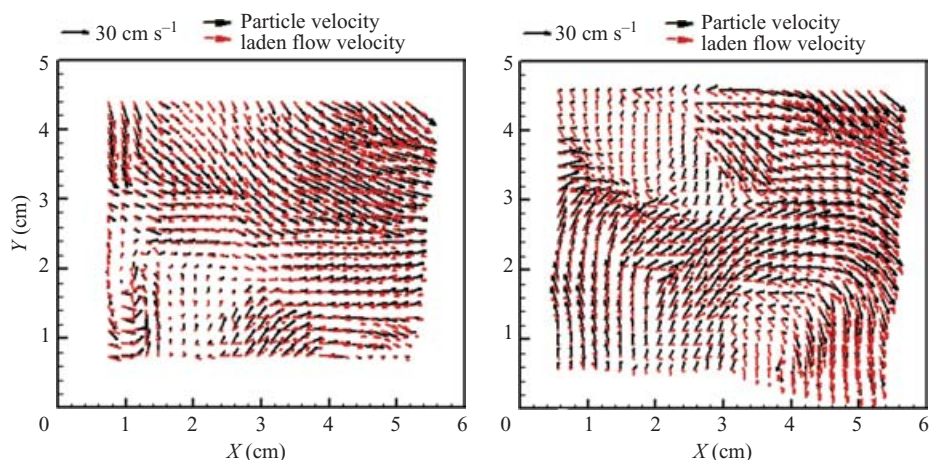

FIGURE 18. The laden fluid velocity vector field overlaid by the corresponding particle velocity vector field for (*a*) copper and (*b*) glass particles, at $Re_\lambda = 120$.

particles, respectively. From a comparison between figures 17(*b*) and 17(*d*) for glass particles where $Re_\lambda = 120$ and $St \approx 1.0$, it can be seen that the particles tend to accumulate near low-vorticity regions which in turn allows these particles to cluster along the periphery of intense vorticity structures, corresponding to regions of high strain rates in the laden fluid velocity fields. Similar results can be also observed for copper particles where $St \approx 0.36$ in figures 17(*a*) and 17(*c*). Note that the intense vortical structures of the laden turbulent flow, as clearly shown on figure 17(*d*) with $St \approx 1.0$, appear banana shaped, because the clustered particles accumulating along their periphery may exert particle forces on the fluid and thus stretch these vortical structures of the laden turbulent flow in the gravitational direction. By comparing with the unladen fluid shown in figure 3 at the same $Re_\lambda = 120$, the gravitational stretch on the intense vortical structures of the laden fluid due to particle forces is clearly observed from figure 17(*d*). This experimental evidence supports the recent numerical work by Ferrante & Elghobashi (2003) who examined two-way coupling in particle-laden isotropic turbulence and reported similar banana-shaped vortical structures.

Since we have obtained the evolution of both the particle velocity (V_p) and the corresponding laden fluid velocity (u) fields, as shown on figure 18 as a typical example, the slip velocities between the descending particles and the surrounding fluid can be calculated, including $|(V_p - u)|$ and $|(u - v_p)v_p|$ where v_p is the instantaneous fluctuating velocity of the descending particles, $v_p = V_p - \langle V \rangle_{s,\perp}$, and $\langle V \rangle_{s,\perp}$ is the mean particle settling velocity in the gravitational direction. Both slip velocities are then normalized by the energy-weighted turbulent intensity as $|(V_p - u)|/u'$ and $|(u - v_p)v_p|/u'^2$, respectively. These two normalized slip velocities are directly related to the energy production and loss in the presence of heavy particles, as will be discussed in the next subsection. Figure 19 displays the p.d.f. of these two normalized slip velocities for three different heavy particles with values of St of 0.36, 1.0 and 1.9, respectively. Each p.d.f. curve on figure 19 contains 9216 data samples from points (*a*–*i*) (figure 3). As can be seen, these slip velocity increase with the particle inertia and body force. The larger the slip velocity, the larger the local drag of the particles. If the energy production is larger than the energy dissipation in the presence of these heavy particles, turbulence augmentation should occur. The slip velocities data on figure 19 will be used to investigate turbulence modification, as discussed below.

4.5. *Turbulence modification*

4.5.1. *Wavelet energy spectra of laden turbulent flow*

Applying exactly the same wavelet analyses to these particle-laden fluid velocity signals as to the unladen fluid velocity field, the averaged wavelet frequency spectra for particle-laden flows using equation (6) can be obtained. Again, in an attempt to make the spectra coincide as closely as possible with continuous phase measurements, we calculate the laden turbulent kinetic energy frequency spectra in the Eulerian reference frame from points ((*a*–*i*) on figure 3) over the measurement field of 5.84 cm × 5.11 cm (the region of interest). Each of the nine points contains 1024 temporal data samples giving a total of 9216. These results are presented in figures 20, 21, and 22, respectively for copper particles with $St \approx 0.36$, glass particles with $St \approx 1.0$, and lead particles with $St \approx 1.9$, where all three cases have the same $Re_\lambda = 120$. Each of these three figures shows both horizontal (*a*) and vertical (*b*) components of the energy spectra in which both unladen and laden data are plotted together for comparison. Note that the unladen energy spectra in the horizontal and vertical directions are from figure 6. Also plotted are three characteristic time scales of turbulence at $f = 7\,\mathrm{Hz}$
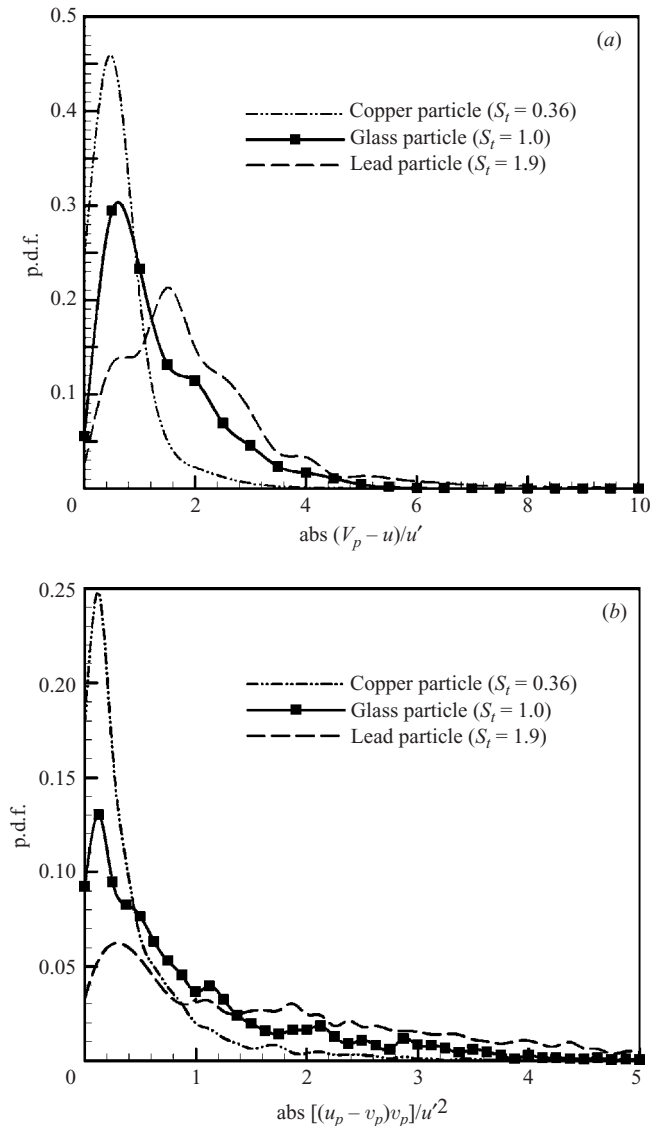
FIGURE 19. The probability distribution of the two slip velocities for three different heavy particles: (a) $|(V_p - u)|/u'$ and (b) $|(u - v_p)v_p|/u'^2$, where the experimental conditions are $f = 7\,\mathrm{Hz}$ and $Re_\lambda \approx 120$.

and $Re_\lambda = 120$, namely the integral, Taylor, and Kolmogorov time scales, τ_I, τ_λ, and τ_k, respectively, see table 1.

It can be seen from figure 20 that when the characteristic frequency is within the range from τ_I^{-1} to τ_λ^{-1}, the particles with weak inertia and body forces ($St \approx 0.36$) correspond reasonably well with the fluctuation of fluid turbulence in the inertial range in which the energy spectra are roughly the same for unladen and laden turbulent flows for both horizontal and vertical components. Note that the energy augmentation due to the presence of copper particles with $St \approx 0.36$ only occurs at higher frequencies beyond the Taylor scale (τ_λ^{-1}) for both horizontal and vertical components. On the other hand, at very low frequencies less than 1 Hz in figure 20,
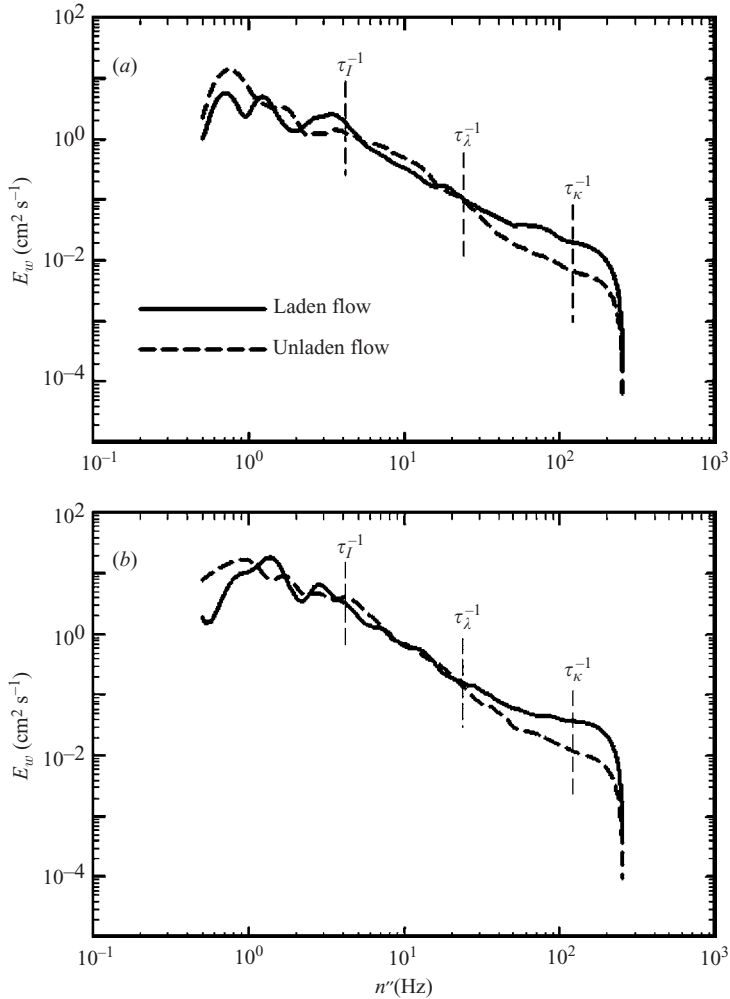
FIGURE 20. The averaged wavelet energy spectra as a function of frequency for copper particles with $St \approx 0.36$ for $f = 7$ Hz and $Re_\lambda \approx 120$. Also plotted are the energy spectra for the unladen flow at the same Re_λ for comparison. (*a*) Horizontal component, (*b*) vertical component.

smaller energy spectra in the laden flow than in the unladen flow are found for both components. The addition of weak-inertia heavy particles to homogeneous isotropic turbulence where $St \approx 0.36$, $Re_\lambda = 120$, and $V_t/V_k = 1$ may even slightly attenuate turbulence energy to be less than that in the unladen turbulent flow at the same Re_λ provided that the characteristic frequency n'' is below 1 Hz.

Figure 21 represents the case of glass particles with moderate inertia and body forces where $St \approx 1.0$, $Re_\lambda = 120$, and $V_t/V_k = 3$. In it there is essentially no turbulence attenuation due to the presence of glass particles over the entire frequency domain for both horizontal and vertical components. In the inertial range around τ_I^{-1}, glass particles with $St \approx 1.0$ correspond very well with fluid turbulence, in which the energy spectra are nearly the same for both laden and unladen turbulent flows. Turbulence augmentation due to the addition of glass particles with $St \approx 1.0$ is clearly observed when n'' is approaching τ_λ^{-1}. This transition frequency (f^*) for which E_w of the laden flow starts to be greater than that of the unladen flow in the case of $St \approx 1.0$ is
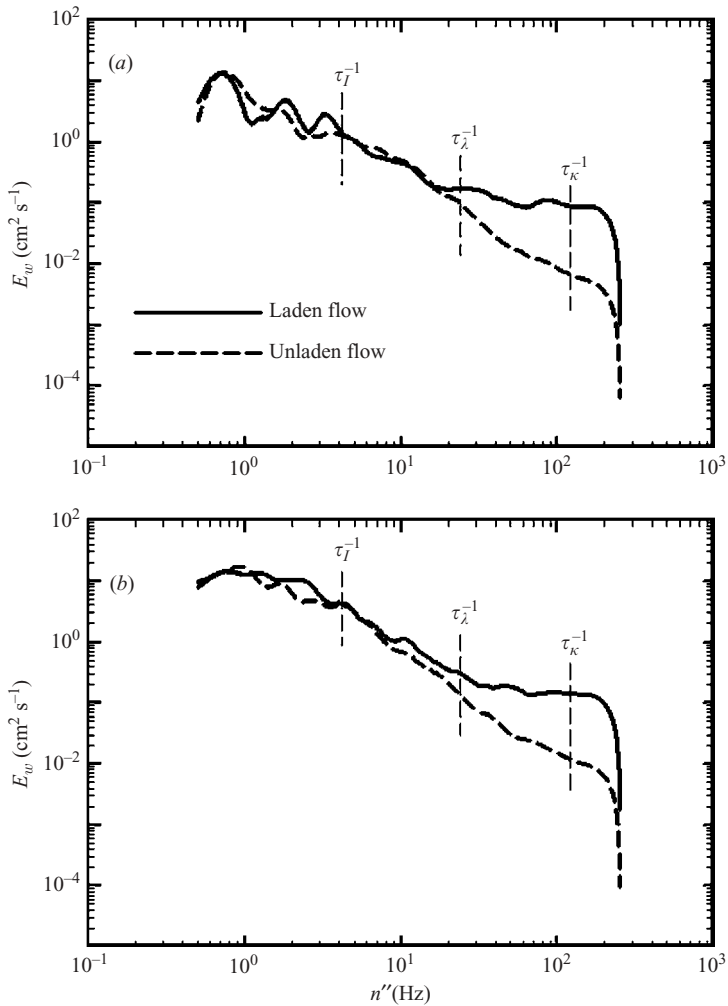
FIGURE 21. Same as figure 20, but for glass particles with $St \approx 1.0$.

much more sensitive in the gravitational direction ($f^* \sim 8\,\text{Hz}$) than in the horizontal direction ($f^* \sim 20\,\text{Hz}$), as can be seen in figure 21. Such a turbulence augmentation due to the two-way interaction between heavy particles and fluid turbulence is much more significant in the dissipation range and reaches its maximum around τ_k^{-1} for both horizontal and vertical components (see figure 21). For lead particles with $St \approx 1.9$, figure 22, similar results are found in the horizontal direction as for glass particles ($St \approx 1.0$) and copper particles ($St \approx 0.36$), in which turbulence augmentation occurs only at higher frequencies in the dissipation range. However, in the gravitational direction, turbulent augmentation of the energy spectra is found over the entire frequency domain for lead particles with $St \approx 1.9$; the larger the inertia and body forces, the larger the slip velocity between particles and fluid turbulence that acts as a feedback force on the laden fluid.

By comparing these energy spectra at τ_k^{-1} among figures 20, 21, and 22, it is found that the maximum turbulence augmentation due to the presence of heavy particles occurs at $St \approx 1.0$ at which the particle preferential accumulation is most significant.
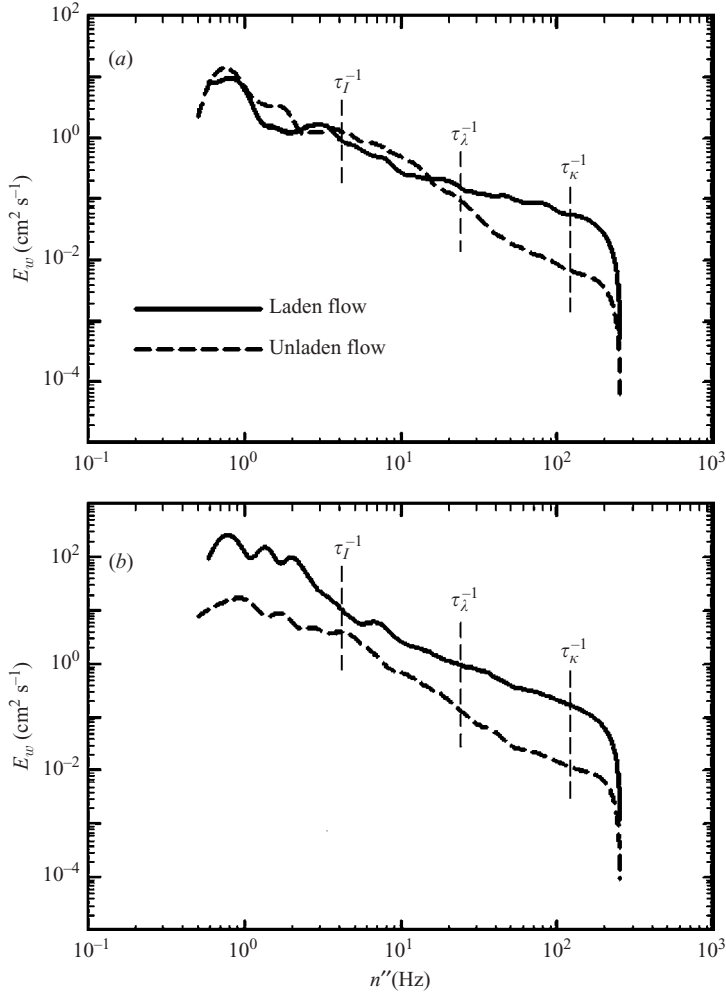
FIGURE 22. Same as figure 20, but for lead particles with $St \approx 1.9$.

These particle clusters can stretch vortical structures they surround to a banana-like shape pointing preferentially in the gravitational direction, as can be seen in figure 17(d). This explains why the mean particle settling rate is maximum when the particle relaxation time is comparable to the Kolmogorov time scale of turbulence at which $St \approx 1.0$. In all, turbulence augmentation in the gravitational direction is found over the entire frequency domain when $St \geqslant 1$, while in the transverse direction turbulence augmentation only occurs at high frequencies beyond the Taylor microscale.

4.5.2. *The flatness factor*

Here we quantify the level of intermittency for both unladen and laden turbulent flows using the flatness factor (see equation (7)) to further investigate the effect of St on the particle settling behaviour. Figure 23 presents the flatness factor F as a function of frequency for both horizontal (a) and vertical (b) components, each including four cases: one for the unladen flow and three for the laden flows with different values of St, where all four cases have the same $Re_\lambda = 120$. As can be seen,
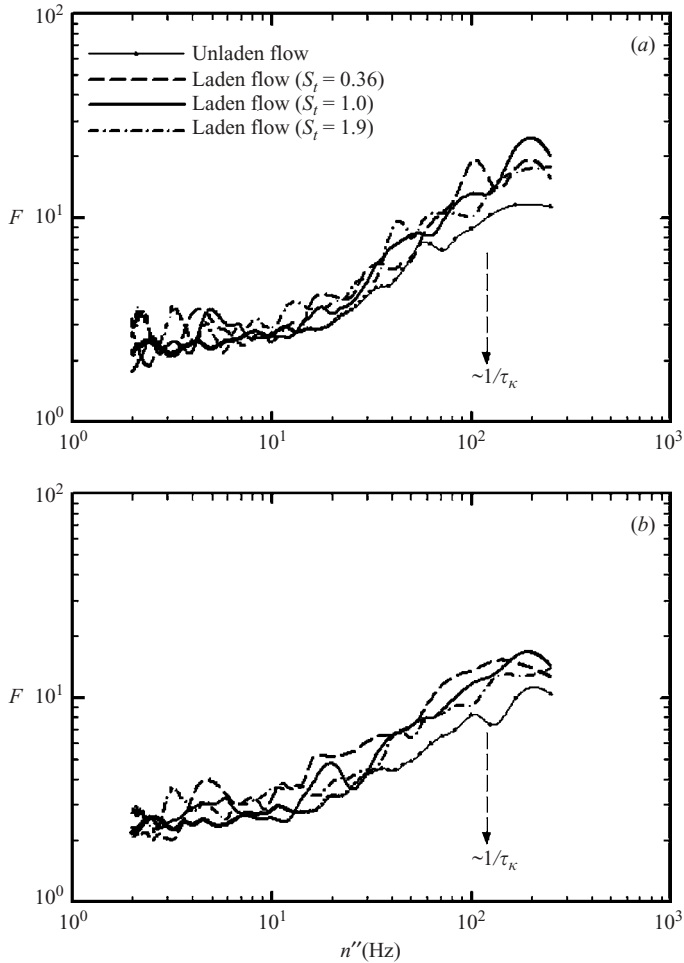
FIGURE 23. The flatness factor F extracted from the time evolution of velocity signals using temporal wavelet analyses for (*a*) horizontal and (*b*) vertical components, each including the unladen case and three laden cases with different values of St, and $Re_\lambda = 120$.

values of F for laden turbulent flows are generally higher than for the unladen case at any given frequency greater than the Taylor microscale (τ_λ^{-1}).

As discussed previously, the larger the value of F is, the higher the level of intermittency is. Therefore, turbulence augmentation due to the presence of heavy particles that exert particle forces on the surrounding fluid to enhance the available energy of laden fluid, in particular at small scales of turbulence, can modify the laden turbulent flow to become more intermittent in the dissipation range. Note that the highest value of F, equivalent to the highest level of intermittency, is found to be in the case of $St \approx 1$ at $n'' \approx 200$ Hz in the dissipation range (see figure 23). This is because the strength of small intense vorticity structures can be enhanced by turbulence augmentation for which the particle preferential accumulation is most intermittent at $St \approx 1$ (see figure 13). Furthermore, values of F for these laden cases are larger in the horizontal direction than in the vertical direction, indicating that the intense vorticity structures in the horizontal direction become more intermittent than in the gravitational direction. This finding supports the aforementioned result of banana-shaped

small intense vortical structures (figure 17*c, d*) that are stretched by the clustered heavy particles and are shifted toward the gravitational direction.

4.5.3. *A modified energy balance model*

Kenning & Crowe (1997) proposed an energy balance concept to predict the effect of solid particles on turbulence in gas–particle dispersion flows, in which the possible production of energy by turbulence (E_i) and the velocity difference between the particles and the fluid (E_p) are balanced by the possible losses of turbulence energy consumed by the viscous dissipation (D_v) and the retransmission of energy to the motion of the solid particles (D_p), given by

$$E_i + E_p = D_v + D_p. \tag{8}$$

It seems reasonable to assume that this energy balance concept could be used in the present settling problem. However, gas–particle dispersion turbulent flows (e.g. turbulent jet and wake flows), have a strong mean flow velocity, and the flows are dominated by large energetic coherent vortices. This differs with the present flow in which mean flow velocities are negligible and small-scale turbulence also plays a role, and thus some modifications are required.

Since the unladen and laden fluid energy-weighted turbulent intensities, u' and u'_l, can be obtained using DPIV and DPIA techniques as discussed previously, the ratio u'_l/u' may be used as an indication of turbulence modification due to the two-way interaction between heavy descending particles and homogeneous isotropic turbulence. Theoretically, u'_l/u' may also be predicted by the four terms in equation (8) after some modifications. For the present turbulence, the first term, E_i, is the inherent turbulence production term in the absence of heavy descending particles that may be estimated by $E_i \approx u'^3/L_1$ as the rate of turbulence production. The second term, $E_p = (f'/\tau_p)(V_p - u)^2$, is the average energy production term due to the velocity difference between the particles and the fluid, where f' is the ratio of the particle drag to the Stokes drag as given by the equation (2) and V_p is the mean velocity of heavy particles. $D_p = (f'/\tau_p)|(u - v_p)v_p|$ is the loss of turbulence energy which is the rate of work done by the laden fluid on the fluctuating motion of heavy descending particles. Note that these three terms, E_i, E_p, and D_p, can be easily determined from table 1 and figure 19 in the present study, where the two slip velocities for each of the three heavy descending particles, $|V_p - u|$ and $|(u - v_p)v_p|$, are selected from the peak values of the p.d.f. distributions on figure 19 and are used to estimate E_p and D_p, respectively. Finally, the viscous dissipation in the presence of heavy particles may be defined as $D_v = u'^3_l/L_H$, where L_H is a hybrid characteristic length scale that may be related to the sizes of the particle clusters and banana-shaped intense vortical structures in the present laden turbulent flow, to be defined as follows.

Hunt (2000) pointed out that the local value of the dissipation rate is most intense either in a vortex sheet or at the outer perimeter of a vortex tube. This view is consistent with an experimental finding on scalar dissipation rate fields measured in an aqueous vibrating-grid turbulence using the three-dimensional laser-induced fluorescence technique (Shy, Gee & Lee 1999), in which the sheet-like/tube-like structures are such that one dimension is much smaller/larger than the other two dimensions, respectively. Similarly, the present particle clusters accumulate around the outer perimeter of intense tube-like structures where the dissipation rate is most intense. These banana-shaped vortical structures have an average diameter on the order of ten Kolmogorov length scales, see §4.1 and §4.4. Furthermore, the characteristic length scale of the particle clusters that accumulate around the outer perimeter of these
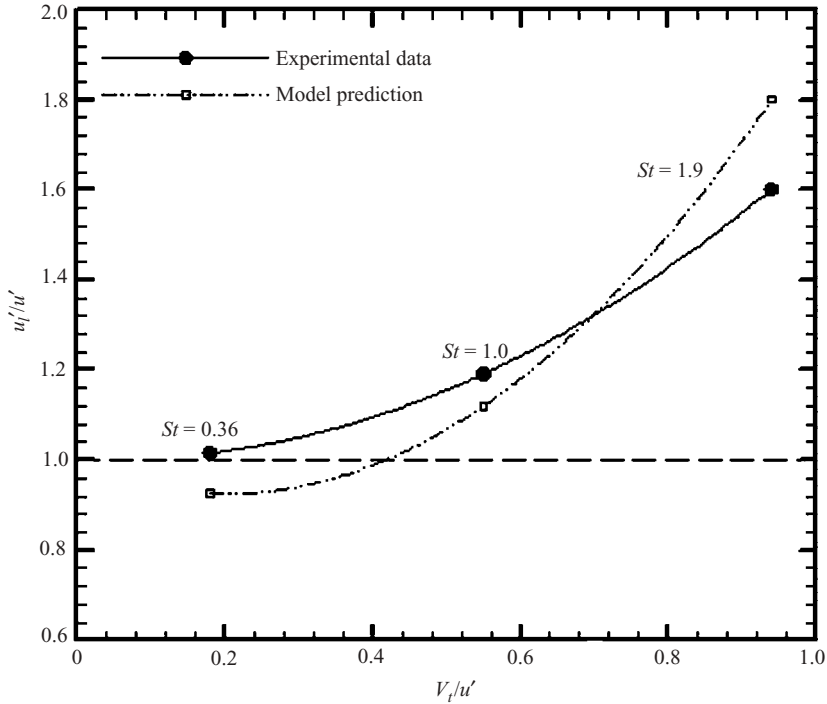
FIGURE 24. The ratio of laden to unladen turbulent intensities as a function of V_t/u', including the present experimental data and the model prediction using (9) for comparison.

tube-like vortical structures is found to be the Taylor microscale, as discussed in §4.2. Hence, the hybrid characteristic length scale may be defined as $L_H = 10\eta + \lambda$ for the present laden turbulent flow. This is reasonable, because the actual characteristic length scale of the laden turbulent flow must take the size of the particle clusters into account as these clusters can turn and stretch the intense vortical structures of the laden fluid toward the gravitational direction and thus increase the settling rate, especially when $St = 1$. From equation (8) and the aforementioned modifications, a modified energy balance model, under the assumption that a stationary state of turbulence can be maintained after the addition of heavy descending particles, is proposed:

$$u'^3/L_1 + (f'/\tau_p)(V_p - u)^2 = (f'/\tau_p)|(u - v_p)v_p| + u_l'^3/(10\eta + \lambda). \tag{9}$$

When the first three terms of this modified energy balance equation as well as the value of $L_H = 10\eta + \lambda$ are determined, u_l' can be predicted using (9).

Figure 24 shows the ratio u_l'/u' function of V_t/u', including both the present experimental data and the model prediction using (9) for comparison. It is found that the trend of the model prediction agrees reasonably well with that of experimental measurements, in which values of u_l'/u' increase with increasing values of V_t/u'. Thus, turbulence augmentation increases as St increases. For instance, experimental values of u_l' are 1.05, 1.20 or 1.60 times greater than u', when $St \approx 0.36$, 1.0 or 1.9, respectively, see figure 24. The best agreement between the model prediction and the experimental data is found to be near $St \approx 1.0$. This is because the preferential particle accumulation is most significant at $St = 1$ and thus the use of $L_H = 10 + \lambda$ in (9) is most accurate.

Generally speaking, turbulence augmentation enhances the mean settling rate because all values of V_s are greater than their corresponding values of V_t, as can be seen on figure 16. However, the largest turbulence augmentation which occurs at $St \approx 1.9$ does not correspond to the highest mean particle settling rate. This can be simply understood from figure 10 where heavy particles with large inertia merely descend without any possible formation of a cluster. The highest mean settling rate value of $(V_s - V_t)/u'$ occurs at $St \approx 1.0$ where the particle accumulation is most significant. Hence, it is concluded that the enhancement of the settling rate due to turbulence is dominated by the formation of particle clusters that can generate forces to turn and stretch intense banana-shaped vortical structures toward the gravitational direction and thus increase significantly the mean settling rate.

5. Conclusions

In the present work, we adopted a novel experimental design which allows direct imaging and velocity measurements of the two-way interaction between solid particles and homogeneous air turbulence. Consequently, DPIV measurements in the cruciform apparatus suitable for qualitative understanding and quantitative analysis of various aspects of particle settling, preferential accumulation, and turbulence modification were obtained for a near-equilibrium state of a turbulent field laden with particles. In itself, we believe that the experimental design is a useful contribution to the study of the particle settling problem. The present measurements and analyses reveal the following.

(i) The most significant preferential accumulation of particle clusters occurs near $St = 1.0$, at which the flatness factor, the level of intermittency, is highest and the p.d.f. distribution of the particle concentration field, $c/\langle c \rangle$, is most non-uniform, as shown on figures 12 and 13, respectively. The characteristic time scale of these particle clusters is equivalent to the temporal passage of these highly clustered structures and is found to be of the order of the Kolmogorov time scale. Furthermore, the characteristic length scale of these particle clusters that distribute themselves along the periphery of intense vortical structures is related to the spacing between the adjacent intense vortical structures and is found to be on the order of the Taylor microscale.

(ii) When $St \sim 1$ and $V_t/v_k \sim 3$, values of $(V_s - V_t)/V_t$ increase significantly from 13% to 38% when values of Re_λ increase from 73 to 202, indicating a strong Re_λ influence on the mean settling rate, as shown on figure 15. The mean particle settling velocity in turbulence is much greater than the terminal velocity in still fluid and the enhanced velocity difference reaches a maximum of $0.13u'$ when $St \approx 1$ and $V_t/u' \approx 0.5$ at $Re_\lambda = 120$ for particles with $Re_p < 1$, in good agreement with previous numerical results. It is found that the settling phenomenon is strongly influenced by intense vorticity structures in which the time and velocity scales that dominate the mean settling rate are τ_k and u', respectively.

(iii) Applying the modified DPIA technique to measure the particle Lagrangian acceleration field and using the Basset–Boussinesq–Oseen equation, the particle-laden fluid velocity field can be obtained. It is found that values of the flatness factor in the horizontal direction of the present particle-laden turbulent flow are larger than in the vertical direction, indicating that the intense laden fluid vorticity structures in the horizontal direction are more intermittent than that in the gravitational direction. By comparing the average wavelet spectra between laden and unladen turbulent flows at a fixed $Re_\lambda = 120$, we found that turbulence augmentation occurs over most of the frequency domain in the gravitational direction especially for $St \geqslant 1$. In the

transverse direction, augmentation occurs only at higher frequencies beyond the Taylor microscale. It is concluded that when $St \approx 1.0$, turbulence augmentation due to the presence of heavy particles in the dissipation range is most significant and reaches its maximum at the Kolmogorov time scale.

(iv) The particle clusters which accumulate preferentially around the outer perimeter of intense banana-shaped vortical structures can turn and stretch these vortical structures toward the gravitational direction and thus significantly increase the mean particle settling rate when $St \approx 1$. That is also the reason why values of F in the horizontal direction are larger than that in the vertical direction for these laden turbulent flows. A simple modified energy balance model for turbulence modification is given to explain these results.

This study provides a full experimental assessment of the particle settling behaviour in stationary near-isotropic turbulence, including the long-time particle concentration field, the mean particle settling rate, and the two-way coupling of the particle–turbulence interaction. In the future, we shall measure experimentally the scaling exponents of nth-order velocity structure functions for n up to 20 to investigate the scaling law of small-scale intermittency in both unladen and laden turbulent flows. Moreover, the present cruciform apparatus can be used to study particle–turbulence interactions at reduced and elevated pressures varied from 0.01 atm to 5 atm, Thus, new results on the influence of aerodynamic drag on the particle settling behaviour in turbulence may be obtained by comparing the spatiotemporal information between low pressure and high pressure cases. We are currently analysing several experiments conducted at either 0.5 atm or 1.5 atm and these results will be reported in the near future.

Appendix

A.1. *About the spatial resolution*

Figure 25 shows a comparison of the probability density function of the average thickness of intense vorticity structures between two different view fields with different spatial resolutions for the two cases presented on the left and right of figure 3, respectively about 0.7 cm for a 40 pixels/interrogation window with a field of view 5.84 cm $\times$ 5.11 cm and about 0.3 cm for a 32 pixels/interrogation window with a field of view 3.14 cm $\times$ 2.75 cm. The high-speed camera is operated at 500 frames s^{-1}, and the intense vorticity structures are identified by very high values of vorticity as displayed as red and/or blue colours in figure 3. We estimate the average sizes of these intense vorticity structures, as schematically shown on figure 25, for both cases in figure 3. Each contains about 250 velocity maps for a recording time of 0.5 s. It is found that the sizes of intense vorticity structures are almost the same for these two different cases, ranging from about 0.2 to 0.5 cm for values of p.d.f. greater than 0.1 with a peak p.d.f. near 0.4 cm, regardless of the different pixel resolutions (figure 25). Therefore, the present spatial resolution can capture information on the characteristic
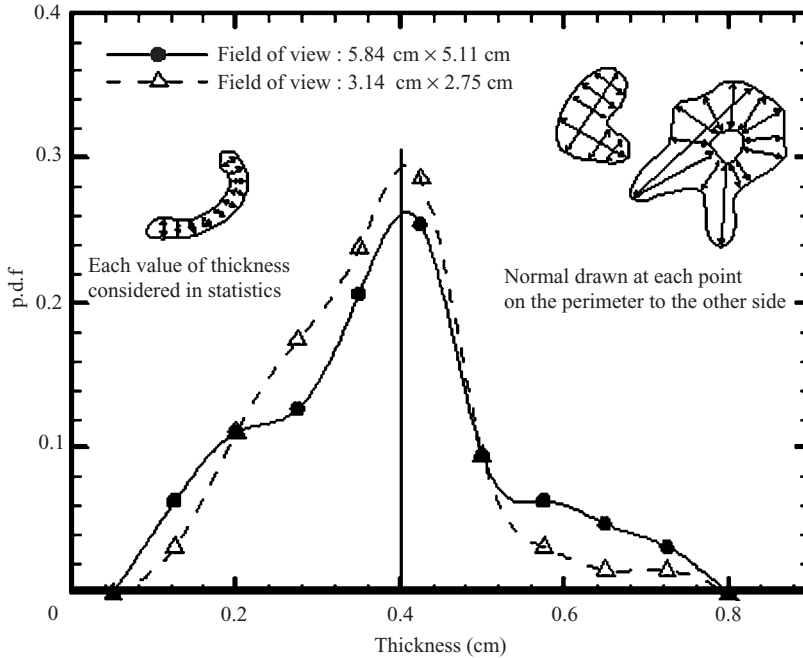
FIGURE 25. Comparison of the probability density function of the average thickness of intense vorticity structures (highest values of vorticity as displayed as red or blue colours in figure 3) between two different view fields with different pixel resolutions.

length scale of intense vorticity structures of turbulence, when the cross-correlation algorithm with recursive local-correlation is used.

A.2. *Validation of the laden fluid velocity field*

Kiger & Lasheras (1995) applied a phase-Doppler particle analyser and Fessler & Eaton (1999) used a laser Doppler velocimeter to measure both laden fluid and particle velocities based on single-point measurements. In order to evaluate the slip velocity between the two phases as well as the energy spectra for the whole laden flow field in the presence of heavy particles with turbulence modification, searching for an adequate measurement that can calculate simultaneously both laden fluid and solid particle velocity fields (not just at a single point) is important and is still an open issue. Recently, Khalitov & Longmire (2002) proposed simultaneous two-phase PIV in a turbulent channel flow to identify objects that are sorted into solids and tracers based on parametric combinations of size and brightness. They calculated solid velocities using particle tracking and gas velocities using cross-correlation PIV, for which turbulence modification is not considered because the number of solids in the flow field is too few. Applying the same concept of parametric combinations of size and brightness, we present experiments seeding with both tracers (aluminium particles of $d_p \approx 0.3\,\mu m$) and solids (lead particles of $d_p \approx 24\,\mu m$) for the case of $St \approx 1.9$ to evaluate the validity of the indirect method using the approximate BBO equation $\rho_p/\rho_f \gg 1$. We present only the case of lead particles because the absence of preferential accumulation at $St \approx 1.9$ is essential for the separation of tracer and solid images in a given flow field with turbulence modification (see also §2.3.3). In the present study, both tracer and solid velocity fields are calculated via DPIV.
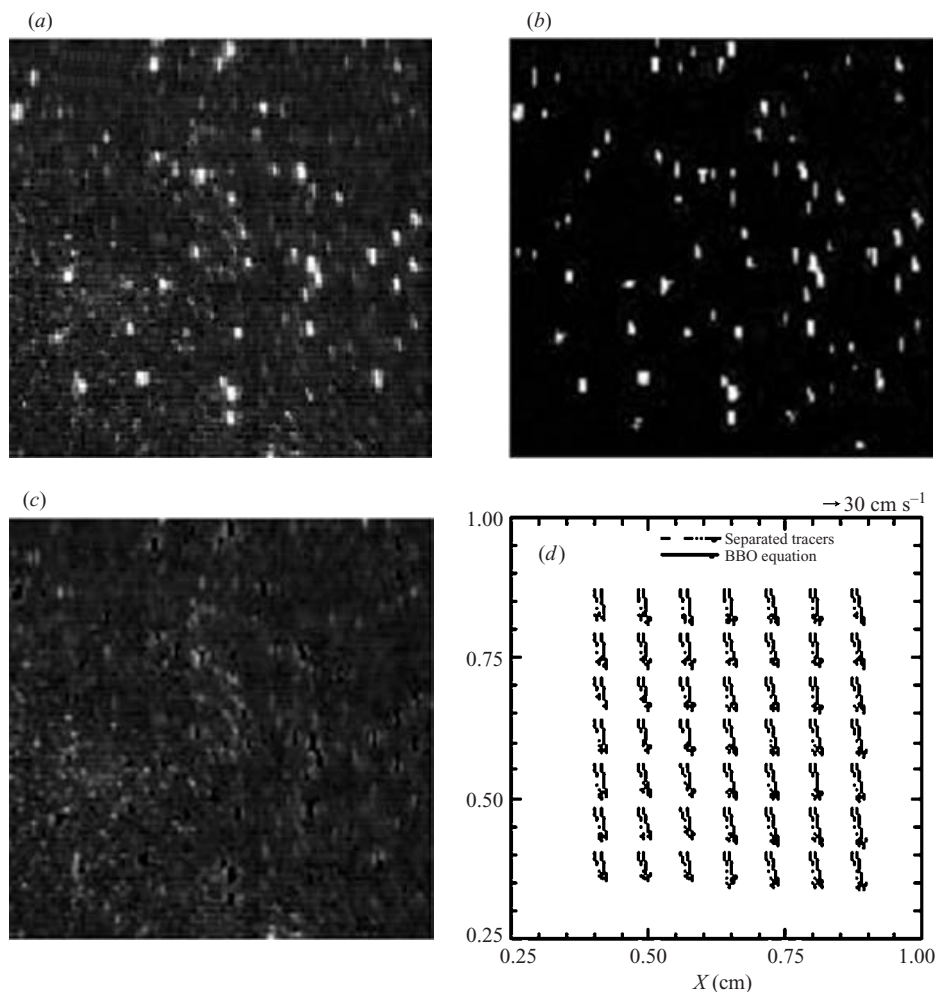
FIGURE 26. Image processing for separation of heavy particles from flow tracer particles and the corresponding particle-laden fluid velocity fields. (*a*) The original two-phase image, (*b*) the separated lead particles ($d_p \approx 24\,\mu$m), and (*c*) the separated aluminium flow tracer particles ($d_p \approx 0.3\,\mu$m). (*d*) Comparison of laden fluid velocity maps measured simultaneously using flow tracer particles (direct measurements) and the heavy particle acceleration field with the BBO equation (indirect measurements) (slightly displaced for clarity), where the experimental conditions are $f = 7\,$Hz, $Re_\lambda \approx 120$, and $St \approx 1.9$.

We now describe the phase differentiation procedure and the validation of separated images for DPIV measurements. As shown on figure 26(*a*), the raw two-phase image of 128×128 pixels with a field of view about $1.25 \times 1.25\,$cm^2 is carefully selected from the original DPIV image of 320×280 pixels with a field of view $3.14\,$cm $\times 2.75\,$cm, where the distributions of both tracers and solids should be as uniform as possible in the image with appropriate amounts of particles. An adequate number of particles is important for successfully separating the tracer image from the solid image while ensuring both phases have enough information for accurate DPIV calculation. Using the image intensity and the spot size methods, similar to Khalitov & Longmire (2002), images of both solids and tracers can be separated from the original two-phase image, as can be seen in figures 26(*b*) and 26(*c*), respectively. Figure 26(*d*) shows a comparison

of laden fluid velocity maps measured simultaneously using flow tracer particles (direct measurements) and the heavy particle acceleration field with the approximate BBO equation for $\rho_p/\rho_f \gg 1$ (indirect measurements), where the experimental conditions are $f = 7\,\mathrm{Hz}$, $Re_\lambda \approx 120$, and $St \approx 1.9$. For clarity, the position of the velocity vectors obtained from the approximate BBO equation is slightly shifted 0.01 cm to the right. It is found that values of horizontal and vertical velocity components for both measurements are nearly identical with no more than 5% difference in the mean. This confirms that the approximate BBO equation for $\rho_p/\rho_f \gg 1$ can be used to estimate an accurate laden flow velocity result, when each interrogation window contains enough heavy particle information. From these experiments, the particle number should be at least 9 in the interrogation window of size of about 0.63 cm × 0.63 cm, a size comparable to the Taylor length scale.

REFERENCES

ALISEDA, A., CARTELLIER, A., HAINAUX, F. & LASHERAS, J. C. 2002 Effect of preferential concentration on the settling velocity of heavy particles in homogeneous isotropic turbulence. *J. Fluid Mech.* **468**, 77–105.

BONNET, J. P., DELVILLE, J., GLAUSER, M. N., ANTONIA, R. A., BISSET, D. K., COLE, D. R., FIEDLER, H. E., GAREM, J. H., HILBERG, D., JEONG, J., KEVLAHAN, N. K. R., UKEILEY, L. S. & VINCENDEAU, E. 1998 Collaborative testing of eddy structure identification methods in free turbulent shear flows. *Exps. Fluids* **25**, 197–225.

CAMUSSI, R. & GUJ, G. 1997 Orthonormal wavelet decomposition of turbulent flows: intermittency and coherent structures. *J. Fluid Mech.* **348**, 177–199.

CHANG, K. A. & LIU, L. F. 1998 Velocity, acceleration and vorticity under a breaking wave. *Phys. Fluids* **10**, 327–329.

CHANG, N. W., SHY, S. S., YANG, S. I. & YANG, T. S. 2001 Spatially resolved flamelet statistics for reaction rate modeling using premixed methane-air flames in a near-homogeneous turbulence. *Combust. Flame* **127**, 1880–1894.

CHRISTENSEN, K. T. & ADRIAN, R. J. 2002 Measurements of instantaneous Eulerian acceleration fields by particle image accelerometry: methods and accuracy. *Exps. Fluids* **33**, 759–769.

CROWE, C. T. 1991 The state-of-the-art in the development of numerical models for dispersed phase flows. *Proc. Intl Conf. Multiphase Flows, Tsukuba, Japan* (ed. G. Matsui, A. Serizawa & Y. Tsuji), vol. 3, pp. 49–60.

CROWE, C. T., SOMMERFELD, M. & TSUJI, Y. 1998 *Multiphase Flows with Droplets and Particles*. CRC Press, Ann Arbor.

CROWE, C. T., TROUTT, T. R. & CHUNG, J. N. 1996 Numerical models for two-phase turbulent flows. *Annu. Rev. Fluid. Mech.* **28**, 11–43.

DONG, P., HSU, T. Y., ATSAVAPRANEE, P. & WEI, T. 2001 Digital particle image accelerometry. *Exps. Fluids* **30**, 626–632.

ELGHOBASHI, S. & TRUESDELL, G. C. 1993 On the two way interaction between homogeneous turbulence and dispersed solid particles. I: Turbulence modification. *Phys. Fluids* **7**, 1790–1801.

FARGE, M. 1992 Wavelets transforms and their application to turbulence. *Annu. Rev. Fluid. Mech.* **24**, 395–457.

FARGE, M., KEVLAHAN, N., PERRIER, V. & GOIRAND, E. 1996 Wavelets and turbulence. *Proc. IEEE* **84**, 639–669.

FERRANTE, A. & ELGHOBASHI, S. 2003 On the physical mechanism of two-way coupling in particle-laden isotropic turbulence. *Phys. Fluids* **15**, 315–329.

FESSLER, J. R. & EATON, J. K. 1999 Turbulence modification by particles in a backward-facing step flow. *J. Fluid Mech.* **394**, 97–117.

FRIEDMAN, P. D. & KATZ, J. 2002 Mean rise rate of droplets in isotropic turbulence. *Phys. Fluids* **14**, 3059–3073.

GUI, L. & MERZKIRCH, W. 1998 Generating arbitrarily sized interrogation windows for correlation-based analysis of particle image velocimetry recordings. *Exps. Fluids* **24**, 66–69.

HART, D. P. 1999 Super-resolution of PIV by recursive local-correlation. *J. Visual.* **10**, 1–10.

HINZE, J. O. 1975 *Turbulence*, 2nd edn. McGraw-Hill.

HUNT, J. C. R. 2000 Dynamics and statistics of vortical eddies in turbulence. In *Turbulence Structure and Vortex Dynamics* (ed. J. C. R. Hunt & J. C. Vassilicos), pp. 192–243. Cambridge University Press.

JAKOBSEN, M. L., DEWHIRST, T. P. & GREATED, C. A. 1997 Particle image velocimetry for predictions of acceleration fields and force within fluid flows. *Meas. Sci. Technol.* **8**, 1502–1516.

JENSEN, A., SVEEN, J. K., GRUE, J., RICHON, J. B. & CRAY, C. 2001 Accelerations in water waves by extended particle image velocimetry. *Exps. Fluids* **30**, 500–510.

JIMÉNEZ, J., WRAY, A., SAFFMAN, P. G. & ROGALLO, R. S. 1993 The structure of intense vorticity in isotropic turbulence. *J. Fluid Mech.* **255**, 65–90.

KENNING, V. M. & CROWE, C. T. 1997 On the effect of particles on carrier phase turbulence in gas-particle flows. *Intl J. Multiphase Flow* **23**, 403–408.

KHALITOV, D. A. & LONGMIRE, E. K. 2002 Simultaneous two-phase PIV by two-parameter phase discrimination. *Exps. Fluids.* **32**, 252–268.

KIGER, K. T. & LASHERAS, J. C. 1995 Effect of the vortex pairing on particle dispersion and inter-phase kinetic energy transfer in a two phase turbulent shear layer. *J. Fluid Mech.* **302**, 149–178.

KULICK, J. D., FESSLER, J. R. & EATON, J. K. 1994 Particle response and turbulence modification in fully developed channel flow. *J. Fluid Mech.* **277**, 109–134.

LONGMIRE, E. K. & EATON, J. K. 1992 Structure of a particle-laden round jet. *J. Fluid Mech.* **236**, 217–257.

MAXEY, M. R. & RILEY, J. J. 1983 Equation of motion for a small rigid sphere in a nonuniform flow. *Phys. Fluids* **26**, 883–889.

MEI, R. 1994 Effect of turbulence on the particle settling velocity in the nonlinear drag range. *Intl J. Multiphase Flow* **20**, 273–284.

MOURI, H., KUBOTANI, H., FUJITANI, T., NIINO, H. & TAKAOKA, M. 1999 Wavelet analyses of velocities in laboratory isotropic turbulence. *J. Fluid Mech.* **389**, 229–254.

RAFFEL, M., WILLERT, C. & KOMPENHANS, J. 1998 *Particle Image Velocimetry: A Practical Guide*. Springer.

SAARENRINNE, P. & OIIRTO, M. 2000 Turbulent kinetic energy dissipation rate estimation from PIV velocity vector fields. *Exps. Fluids* (suppl.), S300–S307.

SATO, Y., HANZAWA, A., HISHIDA, K. & MAEDA, M. 1995 Interactions between particle wake and turbulence in a water channel flow (PIV measurements and modeling for turbulence modification). In *Proc. 2nd Intl Conf. on Multiphase Flow* (ed. A. Serizawa, T. Fukano & J. Bataille), pp. 27–40. Elsevier.

SCHRECK, S. & KLEIS, S. J. 1993 Modification of grid-generated turbulence by solid particles. *J. Fluid Mech.* **249**, 665–688.

SHENG, J., MENG, H. & FOX, R. O. 2000 A large eddy PIV method for turbulent dissipation rate estimation. *Chem. Engng Sci.* **55**, 4423–4434.

SHY, S. S., GEE, K. L. & LEE, E. I. 1999 Three dimensional measurements of fine scale structure in an aqueous vibrating-grids turbulence. *J. Flow Visual. Image Process.* **6**, 177–187 (Also presented at *Eighth International Symposium on Flow Visualization, Sorrento (NA), Italy, September, 1–4, 1998*).

SHY, S. S., I, W. K. & LIN, M. L. 2000a A new cruciform burner and its turbulence measurements for premix turbulent combustion study. *Exp. Thermal Fluid Sci.* **20**, 105–114.

SHY, S. S., LEE, E. I., CHANG, N. W. & YANG, S. I. 2000b Direct and indirect measurements of flame surface density, orientation, and curvature for premixed turbulent combustion modeling in a cruciform burner. *Proc. Combust. Inst.* **28**, 383–390.

SHY, S. S., LIN, W. J. & PENG, K. Z. 2000c High-intensity turbulent premixed combustion: General correlations of turbulent burning velocities in a new cruciform burner. *Proc. Combust. Inst.* **28**, 561–568.

SHY, S. S., LIN, W. J. & WEI, J. C. 2000d An experimental correlation of turbulent burning velocity in a new cruciform burner. *Proc. R. Soc. Lond.* A **456**, 1997–2019.

SNYDER, W. H. & LUMLEY, J. L. 1971 Some measurements of particle velocity autocorrelation function in a turbulent flow. *J. Fluid Mech.* **48**, 41–71.

WANG, L. P. & MAXEY, M. R. 1993 Settling velocity and concentration distribution of heavy particles in homogeneous isotropic turbulence. *J. Fluid Mech.* **256**, 27–68.

WELLS, M. R. & STOCK, D. E. 1983 The effects of crossing trajectories on the dispersion of particles in a turbulent flow. *J. Fluid Mech.* **136**, 31–62.

WILLERT, C. E. & GHARIB, M. 1991 Digital particle image velocimetry. *Exps. Fluids* **10**, 181–193.

YANG, C. Y. & LEI, U. 1998 The role of the turbulent scales on the settling velocity of heavy particles in homogeneous isotropic turbulence. *J. Fluid Mech.* **371**, 179–205.

YANG, S. I. & SHY, S. S. 2002 Global quenching of premixed CH_4/air flames: Effects of turbulent straining, preferential diffusion, and radiative heat loss. *Proc. Combust. Inst.* **29**, 1841–1847.

YANG, T. S. & SHY, S. S. 2003 The settling velocity of heavy particles in an aqueous near-isotropic turbulence. *Phys. Fluids* **15**, 883–889.

YANG, Y., CROWE, C. T. & CHUNG, J. N. 1995 Experiments on particle dispersion in a plane wake. *Wash State Univ. MMO Rep.* 95-7, Pullman, WA.